Model-Assisted Analysis of Sugar Metabolism throughout Tomato Fruit Development Reveals Enzyme and Carrier Properties in Relation to Vacuole Expansion.

Bertrand Beauvoit, Sophie Colombié, Antoine Monier, Marie-Hélène Andrieu, Benoit Biais, Camille Bénard, Catherine Chéniclet, Martine Dieuaide-Noubhani, Christine Nazaret, Jean-Pierre Mazat, et al.

Estimated length: 17.4 pages

Running title (32 characters): **Sugar metabolism in tomato fruit**

Full Title (150 characters):

Model-assisted analysis of sugar metabolism throughout tomato fruit development reveals enzyme and carrier properties in relation to vacuole expansion

Bertrand Beauvoit[a,b,1], Sophie Colombié[a], Antoine Monier[a], Marie-Hélène Andrieu[a], Benoit Biais[a], Camille Bénard[a], Catherine Chéniclet[a,b,c,d,e], Martine Dieuaide-Noubhani[a,b], Christine Nazaret[f], Jean-Pierre Mazat[b,g], Yves Gibon[a]

[a] INRA, UMR 1332 Biologie du Fruit et Pathology, F33883 Villenave d'Ornon Cedex, France
[b] Univ. Bordeaux, 146 rue Léo-Saignat, F-33076 Bordeaux Cedex, France.
[c] Univ. Bordeaux, Bordeaux Imaging Center, UMS 3420, F-33000 Bordeaux, France
[d] CNRS, Bordeaux Imaging Center, UMS 3420, F-33000 Bordeaux, France
[e] INSERM, Bordeaux Imaging Center, US 004, F-33000 Bordeaux, France
[f] Institut de Mathématiques de Bordeaux, ENSTBB-Institut Polytechnique de Bordeaux, F-33600 Pessac, France
[g] IBGC-CNRS, UMR 5095, 1 rue Camille Saint-Saëns, 33077 Bordeaux cedex, France

[1] Address correspondence to bbeauvoi@bordeaux.inra.fr.
The author(s) responsible for distribution of materials integral to the findings presented in this article in accordance with the policy described in the Instructions for Authors (www.plantcell.org) is: Bertrand Beauvoit (bbeauvoi@bordeaux.inra.fr).

Abstract (200 words):

A kinetic model, integrating enzyme activity measurements and subcellular compartmentation, was realistically parameterized to fit the sucrose, hexoses and glucose-6-P contents of pericarp throughout tomato (*Solanum lycopersicum* L.) fruit development. The model was further validated using independent data obtained on domesticated and wild tomato species and on transgenic lines, as well. A hierarchical clustering analysis of the calculated fluxes and enzyme capacities together revealed stage-dependent features. Thus, cell division was characterized by a high sucrolytic activity of the vacuole, whereas during expansion sucrose cleavage was sustained by both sucrose synthase and neutral invertase, associated with minimal futile cycling. Most importantly, a tight correlation between flux rate and enzyme capacity was found for fructokinase and PPi-dependent phosphofructokinase, during cell division, and for sucrose synthase, UDP-glucopyrophosphorylase and phosphoglucomutase, during expansion, thus suggesting an adaptation of enzyme abundance to metabolic needs. In contrast, for most of enzymes, flux rates varied irrespectively of enzyme capacities, and most enzymes worked at less than 5 % of their maximal catalytic capacity. One of the major outcomes of the modelling was the quasi exclusive localization of soluble sugars within the vacuole, together with organic acids, thus enabling the osmotic-driven vacuole expansion that was described during cell division.

INTRODUCTION

The development of fleshy fruits, such as tomato (*Solanum lycopersicum* L.), is classified into three distinct but overlapping phases: cell division, in the very early days following anthesis, cell expansion and lastly, maturation. Because most of the cell volume is occupied by a large central vacuole, it has been postulated that fruit growth mainly depends on osmotic-driven enlargement of vacuoles, thereby conferring its fleshy characteristics to the fruit (Ho, 1996). However, stage-dependent changes in the vacuole volume during growth are up to date not fully documented. This issue is particularly relevant since other evidence links fruit expansion to the endoreduplication-caused enlargement of nuclei within mesocarpic cells (Gonzales et al., 2007). Vacuole is important for fruit quality because compounds responsible for the taste and flavors of fruits, such as sugars, organic acids and secondary metabolites, are stored within this organelle (for review Martinoia et al., 2007). A strong sugar transport activity to fruit vacuoles has therefore to be assumed (Shiratake and Martinoia, 2007). However, our knowledge of sugar transporters of the tomato fruit tonoplast, in terms of capacity, specificity and energy requirement, is still limited (e.g. Milner et al., 1995) and *in vitro* experiments are hardly extrapolatable within the framework of metabolic changes that underlie fruit development.

For decades, targeted studies, based on reverse genetics and enzyme purification, have focused on the functional and biochemical characterization of small sets of enzymes of sucrose and starch metabolism. Accordingly, up- and down-regulation of sucrose synthase, which catalyses a potentially reversible reaction in tomato (Sun et al., 1992), brought evidence that this enzyme could be rate-limiting for sucrose cleavage and thus, may regulate sink strength during early fruit development and, ultimately, set the final fruit size (Sun et al., 1992; D'Aoust et al., 1999; Wang et al., 1993; N'tchobo et al., 1999). However, down-regulation of the vacuolar acid invertase (Klann et al., 1996) and of the proton-pumping ATPase (Amemiya et al., 2006) has been shown to increase the sucrose-to-hexose ratio and to decrease the fruit growth rate and size. Conversely, sucrose phosphate synthase (SPS) and neutral invertase have been postulated to play a minor role because of their very low abundance in the tomato fruit. For instance, overexpression of SPS increased the sucrose turnover suggesting that this activity may be a limiting step in sucrose synthesis in domesticated tomato fruit (Nguyen-Quoc et al., 1999). On the other hand, intensive investigations of the related tomato species further emphasized the role played by acid invertase and SPS in the sucrose-accumulating trait of mature wild-type tomato (Miron and

Schaffer, 1991; Dali et al., 1992), thus suggesting the existence of the so-called sucrose cycling during the maturation phase (Dali et al., 1992 and for review, Nguyen-Quoc and Foyer, 2001). Meanwhile, pioneering applications of the Metabolic Control Analysis (MCA) to plant biology illustrated that the influence of a particular enzyme cannot be solely inferred from its over- or under-expression, and that all enzymes and metabolites in the system must be considered (e.g. Thomas et al., 1997).

Given the recent development of 'omics' approaches, correlation network analysis of fruit metabolism during growth and ripening has been performed at the level of transcripts and metabolites (Carrari et al., 2006; Mounet et al., 2009), transcripts and enzymes (Steinhauser et al., 2010), transcripts, proteins and metabolites (Osorio et al., 2011) and, more recently, metabolites and enzymes under challenging environmental conditions (Biais et al., 2014). These integrated approaches revealed the existence of stage-dependent metabolic shifts and, more specifically, led to the identification of gene- and enzyme-subsets that may be implicated in metabolic reprogramming. For instance, hierarchical clustering showed that cell division is characterized by a relative abundance of enzymes involved in the energy metabolism, whereas anaplerotic enzymes were rather abundant during cell expansion (Biais et al., 2014). Thus, large-scale enzyme profiling provides critical information about the metabolic capacity of cells in a given genetic, developmental or environmental context. However, to what extent metabolic fluxes readily respond to enzyme reprogramming remains to be elucidated. In the absence of yet validated protocol of ^{13}C metabolic flux analysis within a developmental series, one strategy of integrating enzyme capacities and metabolic traits is kinetic modelling. This approach has been successfully applied to the Calvin cycle (Pettersson and Ryde-Pettersson, 1988; Poolman et al., 2000) and to sucrose metabolism in sugarcane (Rohwer and Botha, 2001; Uys et al., 2007). Lately, taking into account the properties of tonoplastic proton-pumps and carriers, a kinetic model fairly fitted the evolution pattern of malate in the developing peach fruit (Lobit et al., 2006).

The objective of this work was to give new insights into the control of sucrose metabolism throughout tomato fruit development. For this, we built up a kinetic model of sugar metabolism of pericarp by integrating the subcellular compartmentation and enzymes properties. Simulations were performed throughout fruit development to fit the measured variations of soluble sugar contents. A sensitivity analysis of the calculated fluxes and concentrations was performed to quantify the control exerted by enzymes within the network. Finally, hierarchical clustering was used to unravel hidden properties of the network by linking fruit growth, vacuole expansion, sugar storage and enzyme properties.

RESULTS

Fruit Growth, Cell and Vacuole Expansion throughout Fruit Development

Tomato (*Solanum lycopersicum* var. Moneymaker) fruit growth follows a sigmoidal curve (Figure 1A), which is classically divided in a period of rapid cell division (0 to 10 Days Post Anthesis (DPA)), followed by cell expansion (10 to 44 DPA) and then ripening (Mounet et al., 2009). The volume of the parenchyma cells of pericarp and of their subcellular compartments has been estimated by a morphometric analysis. The mean cell volume was rather small during the division phase and tremendously increased during the expansion phase (Figure 1B). Meanwhile, the vacuolar and cytoplasmic volume fractions within cells changed with time, following a mirror-shaped pattern, *i.e.* between 2 and 15 DPA, the vacuole expanded from about 20 to 75 % whereas the cytoplasm shrank from about 65 to 10 % of the cell volume. Finally, the residual space, mainly occupied by cell wall, remained constant (Figure 1C). Moreover, the plastid-to-cytoplasm volume ratio did not significantly change with time and was equal to 0.13 ± 0.04. In pericarp, the division phase is therefore characterized by an expansion of the vacuole within dividing cell, whereas the fruit expansion phase results in a concomitant increase in all subcellular volumes. Therefore, water movements into the vacuole originate from two phenomena: (i) a non-growth associated vacuole expansion (i.e. volume readjustment between cytoplasm and vacuole) and, (ii) a growth-associated cell expansion (i.e. water flow from phloem to pericarp cells). Consistently, the net water flow across the tonoplast, expressed in µmol of H_2O min^{-1} g^{-1} Fresh Weight (FW), corresponding to each phenomenon was estimated using the vacuole expansion rate derived from Figure 1C (see equation 1) and the fruit growth rate, derived from Figure 1A, times the vacuole volume fraction (see equation 2), as follows:

$$\frac{d\ H_2O_{vacuole\ expansion}}{dt} = \frac{\mathrm{d\,V_{vac}}}{dt} \mathrm{x} \frac{1}{d_{tissue}} \mathrm{x} \frac{d_{water}}{MW_{water}} \qquad \text{eq. 1}$$

$$\frac{d\ H_2O_{cell\ expansion}}{dt} = \frac{\mathrm{dFW}/d_{tissue}}{dt} \mathrm{x} \frac{\mathrm{V_{vac}}}{FW} \mathrm{x} \frac{d_{water}}{MW_{water}} \qquad \text{eq. 2}$$

where d_{tissue} *and* d_{water} are the tissue (in g FW mL^{-1}) and water density, respectively; MW_{water}, the water molecular weight; V_{vac}, the vacuole volume fraction and *FW*, the fruit fresh weight.

Figure 1D shows that the water inflow linked to vacuole expansion was the highest at early stage and constantly decreased during cell division. Meanwhile, the water inflow associated with cell expansion followed a bell–shaped pattern with a maximal value for 15-DPA aged fruit. In sum, major part of water flow into the vacuole was associated with cell

expansion, albeit vacuole expansion *per se* accounted for at most 40 to 25% of the total water movement across tonoplast during cell division (i.e. 4 to 10 DPA) (Figure 1D). The question is therefore to understand the relationships between the stage-dependent water movements into the vacuole and the concentration of sugars and organic acids into this organelle. According to the general principles of kinetic modelling applied to plant metabolic networks (for reviews, Schallau and Junker, 2010; Rohwer, 2012), these cytological data will below be combined with enzyme data sets to parameterize mechanism-based models. Ultimately, it will give access to the carbon import, inter-conversion rates and metabolite concentrations within cell compartments.

Sugar Model Construction and Parameterization

A kinetic model of the carbohydrate metabolism of pericarp cells has been built up according to Figure 2. The core of the network was based on the sugarcane model of sucrose metabolism developed by Rohwer and Botha (2001) and modified by Uys et al (2007). The main implementation was the addition of the vacuole, containing acid invertase (AI) as well as tonoplastic carriers (the mono- and disaccharide carriers), and the plastids, where starch synthesis occurs, containing the glucose-6-P / Pi translocator (Flügge et al., 2011). In addition, the impact of mass increase during growth was taken into account by adding output fluxes at the level of the most abundant cell constituents, namely glucose (Glc), fructose (Fru), sucrose (Suc), starch and polysaccharides of the cell wall. These fluxes were calculated by multiplying the concentration of these compounds by the relative growth rate derived from Figure 1A. Note that the starch turnover, the cell wall invertase activity and the apoplastic hexose import, which are likely to occur at the end of fruit expansion (Nguyen-Quoc and Foyer, 2001), were not included in the model because of a lack of knowledge of their kinetic properties. Finally, glycolysis was the last output flux represented by the aldolase (ALD) reaction (Figure 2).

The model consists of thirteen differential equations (see supplemental Table 5) describing the variations of hexoses, hexoses-phosphates and Suc as a function of the twenty-four enzyme reactions of the network (Figure 2 and see supplemental Table 3). The parameterization of the model was based on our measurements and on the literature. In general, half saturation constants, or Michaelis constants (K_m), from the literature are more reproducible than maximal velocities (V_{max}), as they do not depend on enzyme concentration. K_m values also tend to remain in the same order of magnitude across related species (see e.g. Brenda database, http://www.brenda-enzymes.org). For these reasons, after extensive

reviewing, K_m from different sources have been used, though preferably from studies in tomato or alternatively from other plants (see supplemental Table 4) and their values were assumed to be constant all along fruit development. Moreover, time-dependent functions of the fruit relative growth rate, the subcellular volumes (Figures 1A and 1C) were fitted by a logistic equation. The enzyme capacities (V_{max}) and the metabolite contents of pericarp were determined by fitting data obtained with Moneymaker (Biais et al., 2014) using cubic polynomials (see supplemental Figure 1). The vacuolar ΔpH, estimated from the malate *plus* citrate content of the pericarp, was kept constant throughout the growth period (see supplemental Figure 2). The ATP and ADP contents were assayed on the same samples and the cytoplasmic concentrations subsequently calculated (see supplemental Figures 3A and B). Total acid extractable Pi was almost constant during development (see supplemental Figure 3C) and as shown *in vivo* by ^{31}P NMR (Rolin et al., 2000) Pi concentration was assumed to be the same in cytoplasm and vacuole.

The biochemical reactions, rate equations, parameter settings and corresponding references are listed in supplemental Tables 1 to 4. More particularly, glucokinase (GK) and fructokinase (FK) were parameterized as irreversible Henri-Michaelis-Menten (HMM) (Deichmann et al., 2014) mechanisms, with a competitive Fru, glucose-6-P (Glc-6P) and fructose-6-P (Fru-6P) inhibition of GK (Claeyssen and Rivoal, 2007). Neutral and acid invertases (NI and AI, respectively) were parameterized as irreversible HMM processes, with a competitive and a non-competitive inhibition by Fru and Glc, respectively (Sturm, 1999). Moreover, the vacuolar sucrose- and hexose-H^+ antiporters were parameterized as reversible and symmetrical HMM processes, driven by a proton motive force, with a competition of equal strength between Fru and Glc for the hexose carrier. Considering the pH difference across the tonoplast (ΔpH) as the main component of the proton motive force (Shiratake and Martinoia, 2007), a driving force (i.e. $10^{\Delta pH}$) was introduced in the Haldane relationships, which relate the kinetic parameters of the enzymes to the equilibrium constant of the reactions.

Model Fitting and Validation

The model covered the period of fruit growth, starting at 4 DPA where cell proliferation was active, and ending at 47 DPA where cell expansion ceased. The system of differential equations was solved at ten stages describing the pericarp growth as a succession of quasi stationary states. The concentration of each intermediate is constant at each stage but

may vary from one stage at steady state to another. The initial parameterization of the model left aside three unknown parameters, *i.e.* the sugar carrier capacities, namely V_{max} *10 and* V_{max}*15* (which is equal to V_{max}16), and the Suc import (V1). The values of these three parameters were optimized at each stage by fitting the experimentally measured Glc, Fru, Suc and Glc-6P contents. Briefly, parameter values were randomly searched by least square minimization. The whole iterative process was repeated using randomized initial conditions and the 300 to 400 best scoring combinations of parameters were kept for each stage. Two means of comparing simulations and experiments were undertaken. Firstly, for each parameter combination, Glc, Fru, Suc and Glc-6P contents were calculated. The resulting 300 to 400 values were averaged and superimposed with measured values. Figures 3A to C show that averaged values of Glc, Fru and Suc were fairly close to the measured ones, regardless of the fruit stage. Secondly, as in Baker et al (2010), a new set of parameters was built from the median values of the 300 to 400 combinations. The model was run with this new set of parameters and the calculated Glc, Fru, Suc and Glc-6P contents were compared with measurements as above. Running the model with the median value of each optimized parameter ended in sugar contents fairly close to the corresponding mean values calculated above, on the one hand, and to the measured values, on the other hand (Figures 3A to C). Even though the general evolution pattern of the calculated Glc-6P was consistent with measurements, strong discrepancies subsisted concerning the values (Figure 3D). However, the mechanism of the Glc-6P / Pi translocator led us to consider the Pi gradient between plastids and cytoplasm (Pettersson and Ryde-Pettersson, 1988; Poolman et al., 2000 and references therein). By introducing this parameter in the rate equation, it became possible to accommodate the measured Glc-6P content of 8- to 40-day aged fruits (Figure 3D). Overall, our optimization routine provided suitable values of the three unknown parameters that allow the model to match experiments throughout the entire growth period. Furthermore, for each of the 300 to 400 parameter combinations, fluxes were calculated and averaged, thus allowing the calculation of their coefficient of variation (i.e. standard deviation-to-mean ratio) as an indicator of flux variability. For most fluxes, the coefficient of variation was lower than 10% in the early and late stages and less than 25% in the middle and end of fruit growth (27 to 40 DPA) indicating that the mean of these fluxes was statistically reliable (Martin and Gendron, 2004). However, flux variability was noticeably high for NI and sucrose synthase (Susy) during the early and late growth stages (up to 50%) and, for the Glc carrier and phosphoglucomutase (PGM), in the intermediary growth stages, indicating that these fluxes were not precisely determined (see supplemental Figure 4).

Cross-validation of the model was carried out using previously published enzyme profiles obtained with Moneymaker at three developmental stages (35, 42 and 49 DPA) (Carrari et al., 2006; Steinhauser et al., 2010). Figure 4A shows a good consistency between the measured and simulated Suc, Fru and Glc contents, regardless of the stage (p-value < 0.05). Likewise, the response of the model towards changes in the sucrolytic enzyme activities was tested using published data obtained on various sucrose-accumulating tomatoes, i.e. on transgenic lines of *L. esculentum* under-expressing AI (Klann et al., 1996), on the wild tomato *L. chmielewskii* (Yelle et al., 1988) and on introgression lines obtained by breeding *L. esculentum* with *L. chmielewskii* (Yelle et al., 1991). Again, a good consistency arose between the measured and the simulated Suc content regardless of the intra- or inter-species modulation of enzyme capacities (p-value < 0.01) (Figure 4B).

The fitting of the three unknown parameters (i.e. Suc import and carrier's V_{max}) and the subsequent validation provided the opportunity to investigate, at the system level, the control of the import, distribution and accumulation of sugars.

Retro-inhibition of Acid Invertase and Glucokinase and Proton-Coupling of the Tonoplast Carriers are Essential for the Model Fitness.

A sensitivity analysis of the model showed that sugar contents were strongly and positively sensitive to both the ΔpH value and the K_m value of the hexose carrier. Conversely, Suc content was strongly and negatively sensitive to the K_i values of AI for Glc and Fru and to the K_m value of the Suc carrier. So was the Glc content to the K_i value of GK for Glc-6P (and not Fru-6P) (see supplemental Figure 5). To further address the respective influence of these parameters on the data fitting, model optimization was carried out as above under conditions where AI and GK were not retro-inhibited by their products. In both cases, a sum of weighted squared errors between calculations and measurements was calculated for each stage as a score of model fitness. Figure 5A shows that the score was drastically high for most growth stages. This was mainly due to differences in Suc or Glc contents in the case of AI or GK parameterization, respectively (see supplemental Figure 6). Similarly, changing the parameterization of carriers from active to passive mechanism (no H^+ coupling) drastically decreased the goodness of fit regardless of the developmental stage (Figure 5A). In this case, it was mainly due to discrepancies between calculated and measured Glc, Fru and Suc contents (see supplemental Figure 6). Overall, this approach tends to demonstrate that both a retro-inhibition of AI and GK and a H^+-coupling of the tonoplast carriers are essential to accommodate the experimentally measured sugar content along fruit development.

Intriguingly, the only K_m values ever published for the tonoplast of tomato fruit are ten- to hundred fold higher than in other species and the energy requirements of Suc and Glc transport remain unclear (Milner et al., 1995). Therefore, the capability of the model to respond to changes in carrier affinity was further tested by scanning the K_m values from sub- to hundred mM ranges. It is worth noting that a change of affinity from high- to low- and very low-affinity only slightly decreased the goodness of fit (Figure 5B), thus making possible to used all three parameterizations for further modelling.

Stage-dependent Changes in Tonoplast Carrier Capacities and in Sucrose Import into Pericarp Cells

Figures 6A and B represent time courses of the carrier's V_{max} predicted by the model under conditions of high-, low- and very low-affinity parameterization. It is worth noting that, for both carriers and regardless of the growth stage, an increase in the K_m values in the model was somehow compensated by an increase in the V_{max} values, *i.e.* the higher the affinity of the carrier, the lower the predicted carrier capacity. Strikingly, V_{max} reached extremely high values (up to 20 µmol min^{-1} g^{-1} FW) when the K_m for hexose and Suc were set at 40 and 120 mM, respectively. Overall, it is remarkable that for both carriers the predicted V_{max} values were high in the division phase, decreased during expansion and, in the case of the Suc carrier, further increased at the end of growth. This evolution pattern was about the same regardless of the carrier's affinity (Figures 6A and B).

The calculated Suc import flux was high during early cell division, sharply decreased during expansion to reach a basal value at the beginning of maturation (Figure 6C). It is worth noting that this trend was not significantly influenced by the parameterization of the carriers. Moreover, the Suc import calculated by the kinetic model was quite consistent with that estimated using the fruit construction cost model of Heuvelink (1995), which estimates the amount of carbon assimilated into biomass and that consumed by respiration throughout the growth period (Figure 6C).

Flux Partitioning Analysis Reveals Stage-dependent Contributions of the Sucrose Cleaving Enzymes

As already pointed out for the Suc import, fluxes within the network did not vary significantly with respect to the affinity of vacuolar carriers. Consequently, in the following section, flux will be presented as the average of values calculated under very low, low and high affinity conditions. Figure 7A represents the splitting of the imported Suc into soluble

sugars, polysaccharides (cell wall and starch) and glycolysis throughout fruit growth. Firstly, fluxes towards soluble sugar and polysaccharides, which were of the same order of magnitude, decreased with time following a sigmoidal shape. Meanwhile, glycolytic flux, which was high during cell division (accounting for about 33% of the total imported Suc in 4 DPA-aged fruit), sharply decreased during cell expansion and accounted for about 75 % of the total imported Suc in 47 DPA-aged fruit.

Most importantly, flux through the three cleaving enzymes, namely AI, NI and Susy, changed with time (Figure 7B). Indeed, during early cell division, Suc was predominantly hydrolysed in the vacuole by AI, with a flux representing about 80% of the total cleavage in 4 DPA-aged fruit. Then, as the vacuolar hydrolysis decreased with time, the NI and Susy fluxes transiently increased, with maximal values in the middle of cell expansion, each representing about 40 to 30 % of the total Suc breakdown. Finally, flux through Susy and NI tended to zero at the end of growth, even though Susy never functioned in the reverse direction. Meanwhile, sucrose phosphate synthase (SPS) flux slightly increased in the middle of cell expansion but remained always low compared to the total Suc breakdown (at most 10 %) (Figure 7B). Overall, Suc synthesis was rather low compared to degradation thus suggesting that the so-called Suc cleavage-synthesis cycle (Nguyen-Quoc and Foyer, 2001) was poorly active regardless of the developmental stage.

Furthermore, the time-courses of the three fluxes upstream of glycolysis are presented in Figure 7C. The phosphorylation of Fru-6P occurred mainly through PPi-dependent phosphofructokinase (PFP) during cell division, and was relayed by a transient increase in the ATP-dependent phosphofructokinase (PFK) flux during expansion. In comparison, the fructose-1,6-*bis*Pase (FBPase) flux was very low regardless of the stage, thus suggesting that the fructose-1,6-*bis*-P synthesis-hydrolysis cycle was almost inactive throughout the entire fruit growth period.

Sucrose Cleavage is mainly Controlled by Sucrose Synthase, Neutral Invertase and the Tonoplastic Sucrose Carrier

To unravel the kinetic control of sugar metabolism, Metabolic Control Analysis was performed by calculating the so-called flux- and concentration control coefficients (Kacser and Burns, 1973; Heinrich and Rapoport, 1974; Reder, 1988). Fluxes through SPS, Susy and NI, in contrast to AI, were strongly controlled by their own activity. For instance, the control coefficient exerted by SPS on its own flux was close to 1 throughout fruit growth, i.e. any increase in SPS activity would produce a proportional effect on flux (see supplemental Figure

8). Likewise, the control of the Susy and NI fluxes by their own activity was elevated (between +0.5 and +1) mainly at the beginning and at the end of fruit growth. In contrast, the AI flux was rather controlled by substrate availability and thus by the tonoplastic Suc carrier, during the expansion phase (about +0.75) (see supplemental Figure 8).

Transport of Sucrose into the Vacuole and its Subsequent Hydrolysis Build up the Osmotic Potential of the Vacuole

The fate of the Suc transported into the vacuole is illustrated in Figure 8A. During early cell division (i.e. 4 DPA) only 25 % of the transported carbon was stored in the vacuole, the remaining being exported to the cytosol *via* the hexose carrier. During cell division and expansion, as the transport of Suc and its subsequent hydrolysis decreased within the vacuole, the hexose efflux fell (Figure 8A), thus increasing the proportion of carbon stored in the vacuole up to 100% for 27- 30- and 35 DPA-aged fruits. In sum, in young fruits, vacuolar sucrolysis shunts the cytosolic Suc cleaving enzymes and feeds the cytosolic metabolism with hexoses. The consequences of this shunt, which is particularly active during division and early maturation, was further analysed in terms of osmotic strength and energy cost. Thus, the net flux of sugar transport across tonoplast was calculated from the Suc influx *minus* hexoses efflux (Figure 8B). Surprisingly, during early division a net sugar efflux occurred which, given the H^+-coupling mechanism of the carriers, corresponded to a net H^+ influx, thus participating to the proton motive force generation. In contrast, during cell expansion, a net sugar influx occurred, thus corresponding to a net H^+ efflux and to a dissipation of the tonoplast energization (Figure 8B). The question is therefore raised as to the consequences of these transport activities on the steady state distribution of sugars on both sides of the tonoplast.

Given the subcellular concentrations calculated by the model, it is worth noting that all the soluble sugars were predicted to be quasi-exclusively localized in the vacuole all through the fruit growth (see supplemental Figure 9), thus suggesting that their contribution to the cytoplasmic osmotic strength was very weak (< 2 mOsm). Conversely, their contribution to the osmotic strength of the vacuole was rather high and almost constant all over the growth period (about 120 to 150 mOsm) (Figure 8C). Moreover, taking into account the electrogenicity of the malate transport across tonoplast, it has been demonstrated in the peach fruit that malate accumulates quasi-exclusively into the vacuole (Lobit et al., 2006). Applying the same approach, consisting in taking into account the subcellular volumes, the pericarp content of malate and citrate, their acid-base dissociation constants and a thermodynamic

equilibrium of the electrogenic anion-channel of the tomato fruit tonoplast (Oleski et al., 1987), similar conclusions could be drawn for the tomato pericarp (see supplemental Figure 9). Given this, the contribution of malate and citrate to the osmotic strength of the vacuole was calculated. Figure 8C shows that the contribution of these organic acids was high in the early division stages (about 100 mOsm) and constantly decreased during fruit growth to stabilize at around 25 mOsm during expansion. In sum, the contribution of sugars and organic acids to the osmotic strength of the vacuole started at a high value in the early division phase (about 260 mOsm) and constantly decreased to stabilize at around 150 mOsm during expansion.

Sugar Accumulation is mainly Controlled by Sucrose Import and by the Tonoplastic Sucrose Carrier

The control of sugar accumulation and, thereby, of the vacuolar osmotic strength, was further analysed by calculating concentration control coefficients. The control exerted by Suc import into pericarp cells on the sugar accumulation was particularly high during cell division (4 and 8 DPA) and at the beginning of maturation (44 and 47 DPA) (at least +1.5) (Figure 8D). Conversely, the control exerted by the Suc tonoplastic transport was particularly high during cell expansion (15 to 44 DPA) (at least +0.6). In this framework, AI did not noticeably control sugar accumulation, and thereby, the osmotic strength of the vacuole, regardless of the growth stage (Figure 8D). In addition, the negative control of sugar accumulation was shared between the relative growth rate and the tonoplastic hexose carrier (up to -0.8) all over the growth period and, to a lower extent, between GK, PFP and Susy (up to -0.4) (see supplemental Figure 10).

Comparative Analysis of Flux and Enzyme Capacity Patterns Reveals Stage-dependent Enzyme Clusters

To compare flux and V_{max} evolution patterns, a two-dimension hierarchical clustering was performed on fluxes and V_{max} together (Figure 9). Whereas the first dimension ranked the developmental stages (columns), three main clusters were found on the second dimension (V_{max} and fluxes): fluxes and activities (i) undergoing a decrease during cell division (e.g. AI, PFP, GK and tonoplast carriers); (ii) a decrease during cell expansion (e.g. ALD, Suc import, NI, FK) and, (iii) a bell-shaped evolution, with a maximal value in the middle of the expansion phase (e.g. Susy, SPS, FBPase and PFK). It is remarkable that the first-cluster fluxes were associated with the rates of vacuole expansion and Suc storage, whereas the

second ones were rather associated with the rates of fruit relative growth, hexose storage and polysaccharide synthesis and, the third ones, with cell expansion rate (Figure 9). All together, these data illustrate the existence of associations between enzyme rates and stage-specific cellular and subcellular events.

Interestingly, flux and V_{max} of Susy, PFP, GK, PGM and UGPase belonged to the same cluster. These trends have been further confirmed by a direct Pearson correlation analysis (*p*-value < 0.01), thus suggesting an adaptation of enzyme capacity to stage-specific metabolic needs. This is far from true for other enzymes, like AI whose abundance increased at the end of growth whereas its flux was maximal during cell division. In fact, most of enzymes whose V_{max} decreased during cell division (cluster 1) had their actual flux rates either in cluster 2 (e.g. NI, FK, ALD) or 3 (e.g. PFK, PGI) (Figure 9).

Measurements of enzyme V_{max} under optimal *in vitro* conditions serve as valid estimates of flux capacities through pathways. Consequently, the flux-to-V_{max} ratio, i.e. the fractional velocity ratio of enzymes, can be used as an indicator of to what extent the enzyme capacity matches or, alternatively, exceeds the metabolic needs in a given steady state (Newsholme and Crabtree, 1986). As expected, this ratio varied with time according to the above mentioned clusters but, overall, most enzymes worked at less than 5% of their maximal capacity throughout fruit growth (Figure 10). Strikingly, the *in vivo* irreversible reactions of PFK, FK and NI exhibited a bell-shaped evolution of the flux-to-V_{max} ratio, with maximal values of about 10 to 20% of the V_{max} in the middle of cell expansion (15 to 35 DPA). Moreover, the velocity ratio of AI and GK peaked at about 5 % of their V_{max} in the early division and middle expansion phase, respectively. Conversely, the thermodynamically reversible reactions of Susy, PFP, PGI, PGM and UGPase worked at less than 1 to 2 % of their maximal capacity regardless of the growth stage (Figure 10).

DISCUSSION

The present work was aimed to analyse the inter-conversion and storage of soluble sugars throughout the growth of tomato fruit. A deterministic kinetic model describing the time course of sugars within pericarp tissue was built by integrating enzyme properties and the subcellular compartmentation of metabolites. In this model only three parameters (V1, V_{max} 10 and V_{max} 15= V_{max} 16) are unknown. Their optimization allowed us to accommodate the sugar contents measured at ten developmental stages and to perform intra- and inter-species cross-validations using independent data sets.

In agreement with a construction cost (process-based) model (Heuvelink, 1995; Liu et al., 2007), it is demonstrated that fruit growth undergoes a concomitant decrease in Suc import and glycolysis during expansion, when expressed on a FW basis. This trend is in accordance with previous results obtained with tomato fruits fed with radiolabelled sugars suggesting that carbon import is high in youngest fruits (N'tchobo et al., 1999; D'Aoust et al., 1999; Baxter et al., 2005; Li et al., 2012). In addition, the decrease in the glycolytic flux is in line with previous results obtained with discs of Moneymaker pericarp collected at 21, 35 and 49 DPA and labelled with ^{14}C Glc (Carrari et al., 2006).

Kinetic Modelling Unravels Unexpected Behaviours of the Vacuolar Sugar Transport Systems

For decades, the kinetic properties of the tonoplastic transport systems have been extensively studied using a variety of techniques. Whereas the specificity, the affinity and the maximum rate (V_{max}) of transport have been measured only in isolated vacuoles or tonoplastic vesicles, most of the time not from fruits (for tomato, Milner et al., 1995; for review, Shiratake and Martinoia, 2007), they differ widely between experiments and species (Martinoia et al., 2007). Therefore, the reported values, expressed either on a protein mass, on a tonoplast area or a volume basis, are hardly convertible into rates per tissue FW (for peach, see Lobit et al., 2006). Our knowledge of sugar transport across tonoplast, especially under *in vivo* conditions, leaves quantitative modelling under-determined. Nevertheless, an optimization routine allowed us to find realistic kinetic parameters (e.g. V_{max}) and plausible mechanisms (e.g. H^+-coupled antiport) for carriers that make calculations matching measurements at each developmental stage. One of the remarkable observations is that the predicted V_{max} of the tonoplast carriers (expressed on a FW basis), as many enzymes of the carbohydrate metabolism (Biais et al., 2014), undergoes a stage-dependent evolution (Figure 5). For instance, a high transport capacity of the Suc carrier characterizes the cell division phase and the beginning of the maturation, thus positioning the V_{max} of this carrier close to that of AI (Figure 9). In addition, a high transport capacity of the hexose carrier characterizes the cell division phase, thus making this carrier one of the members of the largest enzyme cluster, encompassing sugar kinases (FK, GK, PFK, PFP), hexose-P interconverting enzymes (PGM, PGI) and cleaving enzymes (ALD, NI) (Figure 9). Overall, these data bring evidence that tonoplast carriers have to be integrated into the framework of the stage-dependent enzyme reprogramming that occurs during tomato fruit development (Steinhauser et al., 2010; Biais et al., 2014).

Fruit Growth Undergoes Stage-Dependent Changes in Cellular and Subcellular Volumes of parenchyma cells

The cytological analysis of pericarp cross-sections confirmed that fruit growth is characterized by an increase in the volume of parenchyma cells during the expansion phase (Figure 1B). Most importantly, at the subcellular level, it is shown that vacuole expands and, conversely, the cytoplasm shrinks during cell division (Figure 1C). This expansion accounts for a significant part of the total water inflow across the tonoplast between 4 and 10 DPA. The fact that the vacuole expands faster than the cytoplasm in the very young fruits implies that the osmotic strength of these two compartments varies accordingly (see below). Furthermore, this approach emphasizes the importance of knowing the dynamic of the subcellular volume changes to parameterize a model and to carefully interpret metabolomic data. For instance, the ATP and ADP contents, expressed on the FW basis, were shown to decrease with developmental time. However, when expressed on the cytoplasmic volume basis, the ATP and ADP concentrations were shown to transiently increase during cell expansion, with a nearly constant ATP-to-ADP ratio of about 5.2 (see supplemental Figure 3). This is in line with a recent theoretical study demonstrating that a good knowledge of the subcellular compartmentation is a prerequisite for an unbiased metabolomic analysis (Génard et al., 2014).

Cell Division Undergoes Vacuolar Sucrolysis and Sugar-Driven Vacuole Expansion

Given the activity of H^+-coupled sugar carriers, all soluble sugars are quasi-exclusively accumulated (up to 160 mM) into the vacuole throughout the entire growth period. The osmotic effect of sugar storage at the early division stages is further potentiated by the accumulation of malic and citric acid into the vacuole (up to 100 mM) (Figure 8C). In contrast, the contribution of free amino acids to the vacuole osmotic strength is likely to be weak throughout fruit development, i.e. at most 15 to 30 mOsm during division assuming that amino acids are almost totally localized into storage vacuoles (Tohge et al., 2011). Interestingly, the fact that organic acids result from the partial oxidation of sugars, which also provides ATP for the energization of the tonoplast, is in line with the occurrence of turbo metabolism (Biais et al., 2014) and probably compensates for the predicted sugar efflux from the vacuole. Consequently, the osmotic potential of this organelle reaches high levels (the contribution of sugars and organic acids is about -0.6 MPa), corresponding to about two-third of the osmotic pressure of the whole fruit, thus triggering the water inflow within dividing and

expanding cells. Other physiological benefits of this H^+-coupled accumulation of sugars in the vacuole can be hypothesized. It may facilitate the inward transport of apoplastic hexoses into the pericarp cells down their concentration gradient during the late development (Damon et al., 1988) and may be important for fruit growth when less Suc is available for uptake, especially under challenged environmental conditions. In this respect, the fact that sugar accumulation, and thereby the osmotic strength of the vacuole, is highly controlled by Suc import during cell division (Figure 8D) is in line with the reduced fruit size and low sugar content that are observed when Moneymaker tomato plants are grown under shading conditions (Biais et al., 2014).

Special attention should be paid to the role of AI. Indeed, our analysis suggests that this enzyme did not significantly control the rate of Suc cleavage in the vacuole, nor the extent of sugar accumulation into this organelle. This may explain why a hundred-fold decrease in its expression level in tomato is required to detect any effect on the fruit size and on the sucrose-to-hexose ratio (Klann et al., 1996). In this respect, our modelling approach illustrates that a prerequisite for high Suc storage within sucrolytic tissues is a feedback regulation of the AI by hexoses, on the one hand, and of the GK by hexoses-P, on the other hand. Accordingly, such feedback inhibitions have already been used to constraint a model fitting the day-night Suc fluctuation in leaves (Nagele et al., 2010). In fruit, such properties are essential to fit the Suc content of both sucrose- and hexose-accumulating tomato lines (Figure 4), especially during cell division when Suc particularly accumulates (Figure 3C).

The occurrence of a high sucrolytic activity in the vacuole during cell division induces a hexose efflux coupled to a Suc influx that energizes the vacuole membrane and achieves osmolyte homeostasis. This phenomenon enables the achievement of a steady state of sugar transport across tonoplast with a minimal impact on the overall water movement, since these transport rates remain negligible compared to the water inflow (10 vs. 2000 nmol min^{-1} g^{-1} FW in 4 DPA-aged fruit). In contrast, the impact of sugar transports on the vacuole energization might be physiologically significant. Consistently, the division phase is characterized by the highest accumulation rates of organic acids (i.e. 5 to 2 nmol min^{-1} g^{-1} FW between 4 and 15 DPA), in agreement with previous estimations made for peach (Lobit et al., 2006). Interestingly, these values are of the order of magnitude of those calculated for the sugar-linked proton influx (i.e. 9 to 2 nmol min^{-1} g^{-1} FW, see Figure 8B). This indicates that sugar transports might be coupled to other energy-dependent solute transports during cell division. This does not exclude the participation of the tonoplastic H^+-ATPase, which is likely to be active during this phase (Milner et al., 1995, Amemiya et al., 2006). Taken together,

these data suggest a functional interplay between sugars and organic acids stores to trigger the osmotic-driven vacuole expansion during early growth.

Cell Expansion Undergoes Cytoplasmic Sucrose Breakdown and Synthesis with Minimal Substrate Cycle-Linked Energy Expenditure

An interesting outcome of the present model is that the Suc cleavage is mainly sustained by AI during cell division then, relayed by NI and Susy during cell expansion, thus tending to demonstrate, in contrast to previous statements (Sun et al., 1992; N'tchobo et al., 1999; D'Aoust et al., 1999), that each cleaving enzyme contributes to the fruit sink strength. As discussed above, AI participates to the osmotic homeostasis of vacuole during cell division, which confirms the key role played by this enzyme in the osmotic-driven elongation of other sink organs, such as Arabidopsis root and cotton fiber (Wang and Ruan, 2010). Our results also emphasize the potential role played in the tomato fruit by NI, which was usually considered as a "maintenance" enzyme involved in Suc degradation when the activity of other invertases and Susy are low (Winter and Huber, 2000; Nguyen-Quoc, 2001).

Given the fact that Susy has a relatively low affinity for Suc (about 20 to 65 mM in various fleshy fruits), its highest flux rate during cell expansion is associated with a concomitant increase in its catalytic capacity (see also Wang et al., 1993; Biais et al., 2014) and in the cytoplasmic Suc concentration (see supplemental Figure 9). The latter increase during expansion results from a lower vacuolar hydrolysis and, to a minor extent, from a higher SPS rate. However, the extent of this re-synthesis seems not to exceed 10% of the cleavage, thus indicating that the Suc synthesis-breakdown cycle is less active during growth than previously hypothesized (Nguyen-Quoc and Foyer, 2001). Nevertheless, given the high control exerted by SPS on the Suc synthesis, the three- to four-fold induction of SPS during ripening (see supplemental Figure 1) is expected to end with a proportional increase in the Suc synthesis, in addition to the increase in carbon import and the remobilization of starch that occur at ripening (Biais et al., 2014). In the same way, the extent of the Fructose-1,6BP cycle seems also to be very low. Overall, our results suggest that the metabolic shifts underlying fruit development somehow minimize the energy expenditure both in the vacuole during cell division (Suc influx-hexose efflux cycle) and in the cytoplasm during fruit expansion (Suc and Fructose-1,6BP cycles). This energy-saving priority of the fruit growth is further strengthened by the fact that metabolic shifts occur without any significant changes in the energy status, probed by the ATP-to-ADP ratio (see supplemental Figure 3C). At steady-state, the maintenance of this ratio suggests that the ATP-consuming fluxes decline in parallel

to the ATP-synthesizing fluxes (such as glycolysis, see Figure 7A) along fruit development. All together, these data are in line with the decrease in the capacity of the tricarboxylic acid (TCA) cycle and of the lower glycolysis (e.g. pyruvate kinase) that Biais et al. (2014) observed during expansion.

Inherent (enzyme-based) versus Hierarchical (network-based) Control of Sugar Metabolism throughout Fruit Development

To unravel unexpected regulatory aspects of sugar metabolism, an integrated approach was built upon the calculation of flux control coefficients and fractional velocities and upon the comparison of flux and enzyme capacity patterns. Several case studies have been highlighted.

First of all and most interestingly, Susy, together with UGPase, PGM, PFP and GK, belongs to a group of enzymes whose flux increases in parallel to capacity (Figure 9), thus minimizing the changes in the fractional velocity with time (Figure 10) and, in turn, decreasing its control coefficient during cell expansion (see supplemental Figure 4). This behaviour somehow illustrates an adaptation of the enzyme capacity to the metabolic needs at a given stage, such as glycolysis (PFP, GK) and cell wall synthesis (PGM and UGPase) during cell division, and sucrose unloading (Susy) during cell expansion. It should be stressed out that a hierarchical clustering of enzyme capacities, expressed on a tissue protein basis, has previously shown that PFP, PGM and GK are more abundant during the division phase and, Susy and UGPase, during expansion (Biais et al., 2014). Taken together, these data suggest that the close match of the catalytic capacity to flux needs may be due, at least in part, to protein neo-synthesis. Nevertheless, in these correlation analyses, one cannot exclude that post-translational modifications or protein-protein interactions may modulate V_{max} while the enzyme content remains constant. For instance, a Susy isoform has been shown to be phosphorylated and subsequently translocated to the plasma membrane in developing tomato fruit (Anguenot et al., 2006) raising the possibility that UDP-glucose could somehow be channelled into cell wall constituents (Winter and Huber, 2000). Moreover, acid invertases can be inhibited by proteinaceous inhibitors in the tomato fruit (Tauzin et al., 2013), thus interfering *in vivo* with its development and hexose content (Jin et al., 2009).

The remaining enzymes of sugar metabolism exhibit different evolution patterns of flux and capacity, thus making the velocity ratio varying with time. In this framework, NI, FK and PFK belong to a subgroup of irreversible reaction enzymes whose velocity ratio drastically increases during cell expansion (up to 0.2). However, in this context, only NI was

shown to exert a high kinetic control on its own rate. Conversely, PGI, FBPase, SPS and, to some extent, AI, belong to another subgroup of enzymes whose velocity ratio varies with time but remains very low (up to 0.05), thus reflecting an excess of catalytic capacity. Such evolution patterns resemble those noticed in highly glycolytic animal tissues, where the fractional velocity of both hexokinase and PFK is subject to large variations (from 0.001 to 0.9) with increasing physiological loads, whereas that of PGI remains unchanged (Suarez et al., 1997).

Overall, this study underpins that most of enzyme capacities exceed the actual metabolic needs at each developmental stage, even though the amount of most of the enzymes of sugar metabolism dramatically declines during cell division. Similar conclusion has been drawn for the TCA cycle of cultured *Brassica napus* embryos, by comparing enzyme capacities and ^{13}C measured fluxes (Junker et al., 2007). However, readers should be aware that the concept of "flux capacity provision" (Newsholme and Crabtree, 1986) does not automatically imply, firstly, that the reversible reactions with low velocity ratio lie close to equilibrium and does not exert any kinetic control (e.g. Susy and PFP vs. PGI, PGM and UGPase) and secondly, that the irreversible reactions with high velocity ratio exert a high kinetic control (e.g. GK and PFK vs. neutral invertase). In fact, the flux, the fractional velocity, the proximity of the reaction to equilibrium and the control coefficients of individual enzymes are mutually dependent parameters that are differently related to the network kinetic properties (Kruchenberg et al., 1989; Rohwer and Hofmeyr, 2010). Kinetic modelling is a way to calculate all these parameters thus allowing to perform an exhaustive analysis of the network functioning and regulation.

In conclusion, the integration of enzyme capacities, sugar and organic acid concentrations and subcellular compartmentation in a realistic kinetic model increases our understanding of the metabolic reprogramming underlying the tomato fruit development. One of the remarkable features highlighted therein is the high sugar transport capacity of the vacuole during early cell division and, to some extent, at the beginning of ripening, and the energy-saving priority of fruit growth. Further analysis of the respiratory chain components and further model developments connecting the sugar metabolism to the mitochondrial TCA cycle will also be needed to further deepen the interplays between energy metabolism and anaplerosis in the developing fruit. More work will also be needed to identify the genes underlying these tonoplastic transports, as already done for the H^+-coupled symporters involved in the retrieval of apoplastic sugars at the end of expansion and at ripening (e.g. McCurdy et al., 2010). In this context, implementation of the model with these carriers and

the cell wall invertase will help at deciphering the control exerted by these steps on the final sugar accumulation setting, as already suggested by genetic and biochemical experiments (e.g. Fridman et al., 2004; Baxter et al., 2005).

METHODS

Plant Growth, Fruit Harvest and Sample Processing

Growth of the *Solanum lycopersicum* var. Moneymaker cultivar has been carried out as described in Biais et al. (2014). Briefly, about 200 tomato plants were grown under optimal conditions, in a greenhouse according to usual production practices. Flower anthesis was recorded and trusses were pruned at 6 developed fruits. Ten developmental stages, from 4 to 53 DPA (red ripe), were harvested on three different trusses (truss 5, 6 and 7). For each sample, three biological replications were prepared with a minimum of 4 fruits per replication. Samples were prepared by cutting the fruits (after removing seeds, jelly and placenta) in small pieces (approximately 1 cm x 0.2 cm) of pericarp immediately frozen in liquid nitrogen. Frozen samples were then ground into fine powder with liquid nitrogen and stored at -80 °C until analysis. Given the high reproducibility of the biochemical composition of fruit irrespective of the truss (Biais et al., 2014), the analyses performed on the three trusses were averaged at each developmental stage.

Perchloric Acid Extraction and Determination of ATP and ADP and Pi

Frozen tissues (50-100 mg FW) were ground in liquid nitrogen and extracted at 4 °C using 500 µL of 7% (v/v) perchloric acid supplemented with 25 mM Na_2EDTA. The extract was centrifuged for 5 min at 13,000 *g*. The supernatant was quickly adjusted to pH 5.6 to 6.0 using a 2 M KOH-0.3 M MOPS solution. $KClO_4$ precipitate was discarded by centrifugation (5 min, 13,000 *g*). Adenine nucleotides of the supernatant were measured in a luminometer (Bio-Orbit) using the luciferine – luciferase assay (ATPLite Kit, PerkinElmer) according to the manufacturer's instructions and using external ATP standardisation. Total acid extractable Pi was measured on the same perchloric acid extracts using the colorimetric assay described by Cogan et al. (1999).

Cytological Study

Three Moneymaker fruits were collected at each stage (8, 15, 28 and 41 DPA) and fragments (1 to 2 mm-thick) of equatorial pericarp were fixed for 4 h in glutaraldehyde (2.5% (v/v) in 0.1 M (pH 7.2) sodium phosphate buffer) at 4°C. During the first hour of fixation an increasing vacuum (800 to 200 mbar) was applied. The samples were rinsed three times in phosphate buffer and treated for 2 h with osmium tetroxyde (1% (w/v) in 0.1 M phosphate buffer) at 4°C, then with tannic acid (1% (w/v) in water) for 30 min. After three rinses, the samples were dehydrated by an ethanol series, and embedded in Epon 812. Sections (1 µm) obtained with glass or diamond knives were stained with 0.04% (w/v) toluidine blue and photographed using a Zeiss Axiophot microscope coupled to a Spot RTKE digital camera. Cell and vacuole lengths and areas were measured using the Image-J software, using either automatic thresholding or manual or semi-automatic drawing. Subcellular volumes were calculated assuming that cell, vacuole and nucleus are prolate spheroids of radius a, b and c (with a > b = c). Cell wall was assumed to be delimited by two concentric prolate spheroids. Amyloplasts were assumed to be spherical and homogeneously distributed within cytoplasm. Finally, cytoplasm space was determined by difference between the total cell volume and the above calculated volumes. Similar calculations were carried out on three samples of Ailsa Craig fruits collected at 25 and 40 DPA and on previous electron microscopy observations of parenchymal cells of 1, 2 and 10 DPA Ailsa Craig tomato (Mohr and Stein, 1969).

Computer Modelling

Model was constructed from the mass balance equations of the compartmentalized biochemical network drawn in Figure 2. The general form of the differential equations used is:

$$\frac{dC_i}{dt} = \sum_{j=1}^{n} n_{i,j} \cdot v_j \cdot \frac{Vol_j}{d}$$

where C_i is the concentration of the i^{th} species (in µmol g^{-1} FW), $n_{i,j}$, the stoichiometry of the i^{th} species in the reaction j, Vol_j, the volume fraction of the compartment (in mL mL^{-1} tissue) where the j^{th} reaction takes place, d, the tissue density (in g FW mL^{-1} tissue) and v_j, the rate of the j^{th} reaction (mM min^{-1}) involved in the consumption and production of the i^{th} species. The reaction rate equations, taking into account the measured maximal velocity (V_{max}) of the enzymes, the volume space where they are located, and their kinetic parameters, are listed in the supplemental Tables 1 to 4. The set of differential equations, listed in supplemental Table 5, was solved by the Copasi 4.7 software (Hoops et al., 2006) to satisfy the steady state

condition of metabolic intermediates, i.e. dC_i/dt close to zero. A SBML-formatted file of the model is available as supplementary material.

The tissue contents of Glc, Fru, Suc and Glc-6P at steady state were calculated taking into account the local concentrations of the metabolites given by the model, the compartment volume fractions and the tissue density, according to the following equation:

$$[X]_{total} = \frac{[X]_{vac}.V_{vac} + [X]_{cyt}.V_{cyt} + \ X\ _{plast}.V_{plast}}{d}$$

where $[X]_{total}$ is the tissue content of the metabolite X (in µmol g^{-1} FW) and the subscripts *vac*, *cyt* and *plast* symbolize the volume fraction (in mL mL^{-1} tissue) and the steady state concentrations (in mM) for the cytosol, vacuole and plastids, respectively, and *d*, the tissue density (in g FW mL^{-1}). *d* value was calculated from a linear fit of the time course of the fresh-to-dry weight ratio of pericarp (see supplemental Table 2).

Model Parameter Optimization

Parameter optimization was performed using the random search algorithm and by minimizing an *Obj* score, i.e. the sum of the squared residuals weighed by the standard deviation of each measurement, according to the following equation:

$$Obj = \sum_{i=1}^{n} \left(\frac{X_i cal - X_i exp}{\sigma_i exp}\right)^2$$

where Obj is the objective score, *n*, the total number of species, $X_i cal$, the calculated value and $X_i exp$, the experimental value of a particular species X_i and $\sigma_i exp$, its standard deviation. Sets of initial parameter values were randomly generated to avoid finding only local minima. At each developmental stage, the whole iterative process was repeated and the 300 to 400 best scoring parameter sets were kept for further analysis.

Calculation of the Carbon Import into Fruit using Construction Cost Model

The phloem sucrose flux can be calculated as the sum of the assimilate needs for biomass synthesis and respiration, according to the following equations (Heuvelink, 1995):

$$\frac{dC_{sucrose}}{dt} = \frac{dC_{growth}}{dt} + \frac{dC_{respiration}}{dt}$$

$$\frac{dC_{sucrose}}{dt} = \ C_{DW} + \ q_{growth} \ . \frac{dDW}{dt} + \ q_{maintenance}.DW.Q_{10}{}^{(t°-20)/10}$$

where : $dC_{sucrose}/dt$ is the total sucrose import (g of C day^{-1} g^{-1} DW); C_{DW}, the measured carbon content of the pericarp (C_{DW} = 0.413 ± 0.005 g C g^{-1} DW); q_{growth} and $q_{maintenance}$, the

assimilate requirement for growth-linked and maintenance respiration of fruit, respectively (q_{growth} = 0.15 g C g^{-1} DW, $q_{maintenance}$ = 0.004 g C g^{-1} DW day^{-1} at 20°C); Q_{10}, the temperature-dependent coefficient for maintenance respiration (Q_{10} = 2) and t°, the growth temperature (averaged temperature of the culture was 25.4°C) (Heuvelink, 1995; Liu et al., 2007).

Sensitivity and Metabolic Control Analysis

Sensitivity coefficients are defined as the scaled partial derivative of the simulated values with respect to each parameter:

$$S_j^i = \frac{\partial\, lnX_i}{\partial\, lnp_j}$$

where S_j^i is the sensitivy of simulated measurements (X_i) with respect to parameter p_j. Sensitivity coefficients were calculated using the implemented function in Copasi 4.7 and a delta factor of 0.001 for fixed parameters. The same software was used to calculate the flux ($C_{v_j}^{J_i}$) and concentration ($C_{v_j}^{X_i}$) control coefficients of an enzyme, which are defined as:

$C_{v_j}^{J_i} = \frac{\partial\, lnJ_i}{\partial\, lnv_j}$ and $C_{v_j}^{X_i} = \frac{\partial\, lnX_i}{\partial\, lnv_j}$

where v_j is the activity of the targeted enzyme; J_i , a given flux, and X_i , a given metabolite concentration (Kacser and Burns, 1973; Heinrich and Rapoport, 1974; Reder, 1988).

Statistics and Mathematical Regressions

Hierarchical clustering analysis and Heatmap visualization were performed using the TMeV4 software (Saeed et al., 2003), with the correlation-based distance measure and the average linkage clustering method. Linear and non-linear regressions of the experimental data were performed using the solver function of the Microsoft Excel software. Statistical tests were carried out using Student's *t* test, and deemed significant if $p < 0.05$. Coefficient of variation is defined as the ratio between the standard deviation and the mean values (Martin and Gendron, 2004).

Supplemental Data

The following materials are available in the online version of this article.

Supplemental Figure 1. Time courses of enzyme capacities and polysaccharide contents throughout fruit growth.

Supplemental Figure 2. Estimation of the vacuolar pH throughout fruit growth.

Supplemental Figure 3. Time courses of the adenylic nucleotides and phosphate content of pericarp tissue throughout fruit growth.

Supplemental Figure 4. Flux variability as a function of developmental stage.

Supplemental Figure 5. Sensitivity coefficients of the calculated glucose, fructose and sucrose content towards the parameterization of glucokinase, acid invertase and vacuolar carriers.

Supplemental Figure 6. Influence of the parameterization of the vacuolar acid invertase, glucokinase and sugar carriers on the model fitness.

Supplemental Figure 7. Boxplot graphs of optimized values of the vacuolar carrier capacities and sucrose import.

Supplemental Figure 8. Control of sucrose inter-converting fluxes by enzymes.

Supplemental Figure 9. Evolution of the concentrations of sugars and organic acids within the vacuole and cytoplasm.

Supplemental Figure 10. Control of sugar accumulation by enzymes and fruit growth.

Supplemental Table 1. Nucleotide concentrations, vacuolar ΔpH and compartment volumes of the kinetic model.

Supplemental Table 2. Time-dependent function of relative growth rate, metabolites and enzyme capacities.

Supplemental Table 3. Enzymatic steps, reactions and equations rates of the kinetic model.

Supplemental Table 4. Enzymes, reactions and parameters of the kinetic model

Supplemental Table 5. Ordinary Differential Equations (ODE) corresponding to the network of Figure 2.

Acknowledgments

The authors wish to thank their colleagues of the Fruit Biology and Pathology unit (UMR1332) for their valuable contribution during harvests and sample preparation. This work was funded by the Eranet EraSysBio+ FRIM project and by INRA. The cytological part was performed with the contribution of Martine Peypelut on the Plant Imaging pole of the Bordeaux Imaging Center, member of the national infrastructure of France BioImaging.

Author Contribution

B.B., C.C., M.D.N., J.P.M. and Y.G. designed the research; B.B., B.B., C.B., M.H.A., A.M. performed the research; B.B., S.C., C.N. and M.D.N. analyzed the data, and B.B., S.C., J.P.M. and Y.G. wrote the article, which was later approved by all the other authors.

REFERENCES

Amamiya, T., Kanayama, Y., Yamaki, S., Yamada, K., and Shiratake, K. (2006). Fruit-specific V-ATPase suppression in antisense-trangenic tomato reduces fruit growth and seed formation. Planta **223:** 1272-1280.

Anguenot, R., Nguyen-Quoc, B., Yelle, S., and Michaud, D. (2006). Protein phosphorylation and membrane association of sucrose synthase in developing tomato fruit. Plant Physiol. Biochem. **44:** 294-300.

Baker, S.M., Schallau, K., and Junker, B.H. (2010). Comparison of different algorithms for simultaneous estimation of multiple parameters in kinetic metabolic models. J. Integr. Bioinf. **7:** 133-142.

Baxter, C.J., Carrari, F., Bauke, A., Overy, S., Hill, S.A., Quick, P.W., Fernie, A.R. and Sweetlove, L.J. (2005). Fruit carbohydrate metabolism in an introgression line of tomato with increased fruit soluble solids. Plant Cell Physiol. **46:** 425-437.

Biais, B., Bénard, C., Beauvoit, B., Colombié, S., Prodhomme, D., Ménard, G., Bernillon, S., Gehl, B., Gautier, H., Ballias, P., Mazat, J.-P., Sweetlove, L., Génard, M., and Gibon, Y. (2014). Remarkable reproducibility of enzyme activity profiles in tomato fruits grown under contrasting environments provides a roadmap for studies of fruit metabolism. Plant Physiol. **164:** 1204-1221.

Carrari, F., Baxter, C., Usadel, B., Urbanczyk-Wochniak, E., Zanor, M.-I., Nunes-Nesi, A., Nikiforova, V., Centero, D., Ratzka, A., Pauly, M., Sweelove, L.J., and Fernie, A.R. (2006). Integrated analysis of metabolite and transcript levels reveals the metabolic shifts that underlies tomato fruit development and highlight regulatory aspects of metabolic network behavior. Plant Physiol. **142:** 1380-1396.

Claeyssen, E., and Rivoal, J. (2007). Isozymes of plant hexokinase: Occurrence, properties and functions. Phytochem. **68:** 709-731.

Cogan, E.B., Birrell, G.B., and Griffith, O.H. (1999). A robotics-based automated assay for inorganic and organic phosphates. Anal. Biochem. **271:** 29-35

D'Aoust, M.-A., Yelle, S., and Nguyen-Quoc, B. (1999). Antisense inhibition of tomato fruit sucrose synthase decreases fruit setting and the sucrose unloading capacity of young fruit. Plant Cell **11:** 2407-2418.

Dali, N., Michaud, D., and Yelle, S. (1992). Evidence for the involvement of sucrose phosphate synthase in the pathway of sugar accumulation in sucrose-accumulating tomato fruits. Plant Physiol. **99:** 434-438.

Damon, S., Hewitt, J., Nieder, M., and Bennett, A.B. (1988). Sink metabolism in tomato fruit II. Phloem unloading and sugar uptake. Plant Physiol. **87:** 731-736.

Deichmann, U., Schuster, S., Mazat J.-P., and Cornish-Bowden, A. (2014). Commemorating the 1913 Michaelis-Menten paper Die Kinetik der Invertinwirkung: three perspectives. FEBS J. **281:** 435-463.

Flügge U.-I., Häusler, R.E., Ludevig, F., and Gierth, M. (2011). The role of transporters in supplying energy to plant plastids. J. Exp. Bot. **62:** 2381-2392.

Fridman, E., Carrari, F., Liu, Y.-S., Fernie, A.R., and Zamir, D. (2004). Zooming In on a Quantitative Trait for Tomato Yield Using Interspecific Introgressions. Science **305:** 1786-1789.

Génard, M., Baldazzi, V., and Gibon, Y. (2014). Metabolic studies in plant organs: don't forget dilution by growth. Front. Plant Sci. **5:** Article 85.

Gonzalez, N., Gévaudant, F., Hernould, M., Chevalier, C., and Mouras, A. (2007). The cell cycle-associated protein kinase WEE1 regulates cell size in relation to endoreduplication in developing tomato fruit. Plant J. **51:** 642-655.

Heinrich, R., and Rapoport, T.A. (1974). A linear steady-state treatment of enzymatic chains. General properties, control and effector strength. Eur. J. Biochem. **42:** 89-95.

Heuvelink, E. (1995). Dry matter production in a tomato crop : measurements and simulation. Ann. Bot. **75:** 369-379.

Ho, L.C. (1996). The mechanism of assimilate partitioning and carbohydrate compartmentation in fruit in relation to the quality and yield of tomato. J. Exp. Bot. **47:** 1239-1243.

Hoops, S., Sahle, S., Gauges, R., Lee, C., Pahle, J., Simus, N., Singhal, M., Xu, L., Mendes, P., and Kummer, U. (2006). COPASI – a COmplex PAthway SImulator. Bioinformatics **22:** 3067-3074.

Jin, Y., Ni, D.A., and Ruan, Y.L. (2009). Postranslational elevation of cell wall invertase activity by silencing its inhibitor in tomato delays leaf senescence and increases seed weight and fruit hexose level. Plant Cell **21:** 2072-2089.

Junker, B.H., Lonien, J., Heady, L.E., Rogers, A., and Schwender, J. (2007). Parallel determination of enzyme activities and in vivo fluxes in Brassica napus embryos grown on organic or inorganic nitrogen source. Phytochem. **68:** 2232-2242.

Kacser, H., and Burns, J.A. (1973). The control of flux. Symp. Soc. Exp. Biol. **27:** 65–104.

Klann, E.M., Hall, B., and Bennett, A.B. (1996). Antisense acid invertase (TIV1) gene alters soluble sugar composition and size in transgenic tomato fruit. Plant Physiol. **112:** 1321-1330.

Kruckenberg, A.L., Neuhaus, H.E., Feil, R., Gottlieb, L.D., and Stitt, M. (1989). Decrease-activity mutants of phosphoglucose isomerase in the cytosol and chloroplast of *Clarkia xantiana*. Biochem. J. **261:** 457-467.

Li, Z., Palmer, W.M., Martin, A.P., Wang, R., Rainsford, F., Jin, Y., Patrick, J.W., Yang, Y., and Ruan, Y.L. (2012). High invertase activity in tomato reproductive organs correlates with enhanced sucrose import into, and heat tolerance of, young fruit. J. Exp. Bot. **63:** 1155-1166.

Liu, H.-F., Génard, M., Guichard, S., and Bertin, N. (2007). Model-assisted analysis of tomato fruit growth in relation to carbon and water fluxes. J. Exp. Bot. **58:** 3567-3580.

Lobit, P., Génard, M., Soing, P., and Habib, R. (2006). Modelling malic acid accumulation in fruits: relationships with organic acids, potassium, and temperature. J. Exp. Bot. **57:** 1471-1483.

Martin, L., and Gendron, A. (2004). Méthodes statistiques appliquées à la psychologie: traitement de données avec Excel. (Trois-Rivières : Les Editions SMG).

Martinoia, E., Maeshima, M., and Neuhaus, E. (2007). Vacuolar transporters and their essential role in plant metabolism. J. Exp. Bot. **58:** 83-102.

McCurdy, D.W., Dibley, S., Cahyanegara, R., Martin, A., and Patrick, J.W. (2010). Functioal characterization and RNAi-mediated suppression reveals roles for hexose transporters in sugar accumulation by tomato fruit. Mol. Plant **3:** 1049-1063.

Milner, I.D., Ho, L.C., and Hall, J.L. (1995). Properties of proton and sugar transport at the tonoplast of tomato (*Lycopersicon esculentum*) fruit. Physiol. Plant. **94:** 399-410.

Miron, D., and Schaffer A.A. (1991). Sucrose phosphate synthase, sucrose synthase, and invertase activities in developing fruit of *Lycopersicon esculentum* Mill. and the sucrose accumulating *Lycopersicon hirsutum* Humb. and Bonpl. Plant Physiol. **95:** 623-627.

Mohr, W.P., and Stein, M. (1969). Fine structure of fruit development in tomato. Can. J. Plant Science **49:** 549-553.

Mounet, F., Moing, A., Garcia, V., Petit, J., Maucourt, M., Deborde, C., Bernillon, S., Le Gall, G., Colquhoun, I., Defernez, M., Giraudel, J.-L., Rolin, D., Rothan, C., and Lemaire-Chamley, M. (2009). Gene and metabolite regulatory network analysis of early developing fruit tissues highlights new candidate genes for the control of tomato fruit composition and development. Plant Physiol. **149:** 1505-1528.

N'tchobo, H., Dali, N., Nguyen-Quoc, B., Foyer, C.H., and Yelle, S. (1999). Starch synthesis in tomato remains constant throughout fruit development and is dependent on sucrose supply and sucrose synthase activity. J. Exp. Bot. **50:** 1457-1463.

Nagele, T., Henkel, S., Hormiller, I., Sauter, T., Sawoday, O., Ederer, M., and Heyer, A.G. (2010). Mathematical modeling of the central carbohydrate metabolism in Arabidopsis reveals a substantial regulatory influence of vacuolar invertase on whole plant carbon metabolism. Plant Physiol. **153:** 260-272.

Newsholme, E.B., and Crabtree, B. (1986). Maximum catalytic activity of some key enzymes in provision of physiologically useful information about metabolic fluxes. J. Exp. Zool. **239:** 159-167.

Nguyen-Quoc, B., and Foyer, C.H. (2001). A role for 'futile cycles' involving invertase and sucrose synthase in sucrose metabolism of tomato fruit. J. Exp. Bot. **52:** 881-889.

Nguyen-Quoc, B., N'tchobo, H., Foyer, C.H., and Yelle, S. (1999). Overexpression of sucrose phosphate synthase increases sucrose unloading in transformed tomato fruit. J. Exp. Bot. **50:** 785-791.

Oleski, N., Mahdavi, P., and Bennett, A.B. (1987). Transport properties of the tomato fruit tonoplast. II. Citrate transport. Plant Physiol. **84:** 997-1000.

Osorio, S., Alba, R., Damasceno, C.M.B., Lopez-Casado, G., Lohse, M., Zanor, M.I., Tohge, T., Usadel, B., Rose, J.K.C., Fei, Z., Giovannoni, J.J., and Fernie, A.R. (2011). Systems biology of tomato fruit development: combined transcripts, protein, and metabolite analysis of tomato transcription factor (nor, rin) and ethylene receptor (Nr) mutants reveals novel regulatory interactions. Plant Physiol. **157:** 405-425.

Pettersson, G., and Ryde-Pettersson, U. (1988). A mathematical model of the Calvin photosynthesis cycle. Eur. J. Biochem. **175:** 661-672.

Poolman, M.G., Fell, D.A., and Thomas, S. (2000). Modelling photosynthesis and its control. J. Exp. Bot. **51:** 319-328.

Reder, C. (1988). Metabolic control theory: a structural approach. J. Theor. Biol. **135:** 175-201.

Rohwer, J.M., and Botha, F.C. (2001). Analysis of sucrose accumulation in the sugar cane culm on the basis of in vitro kinetic data. Biochem. J. **358:** 437-445.

Rohwer, J.M., and Hofmeyr, J.-H.S. (2010). Kinetic and thermodynamic aspects of enzyme control and regulation. J. Phys. Chem. B **114:**16280-16289.

Rohwer, J.M. (2012). Kinetic modeling of plant metabolic pathways. J. Exp. Bot. **63:** 2275-2292.

Rolin, D., Baldet, P., Just, D., Chevalier, C., Biran, M., and Raymond, P. (2000). NMR study of low subcellular pH during development of cherry tomato fruit. Aust. J. Plant Physiol. **27:** 61-69**.**

Saeed, A.I., Sharov, V., White, J., Li, J., Liang, W., Bhagabati, N., Braisted, J., Klapa, M., Currier, T., Thiagarajan, M., Sturn, A., Snuffin, M., Rezantsev, A., Popov, D., Ryltsov, A, Kostukovich, E, Borisovsky, I., Liu, Z., Vinsavich, A., Trush, V., and Quackenbush, J. (2003). TM4: a free, open-source system for microarray data management and analysis. Biotechniques **34:** 374-378.

Schallau, K., and Junker, B. (2010). Simulating plant metabolic pathways with enzyme-kinetic models. Plant Physiol. **152:** 1763-1771.

Shiratake, K., and Martinoia, E. (2007). Transporters in fruit vacuoles. Plant Biotech. **24:** 127-133.

Steinhauser, M.-C., Steinhauser, D., Koehl, K., Carrari, F., Gibon, Y., Fernie, A.R., and Stitt, M. (2010). Enzyme Activity Profiles during Fruit Development in Tomato Cultivars and *Solanum pennellii*. Plant Physiol. **153:** 80-98.

Sturm, A. (1999). Invertases, Primary Structures, Functions, and Roles in Plant Development and Sucrose Partitioning. Plant Physiol. **121:** 1-8.

Suarez, R.K., Staples, J.F., Lighton, J.R.B., and West, T.G. (1997). Relationships between enzymatic flux capacities and metabolic flux rates: nonequilibrium reactions in muscle glycolysis. Proc. Natl. Acad. Sci. USA **94:** 7065-7069.

Sun, J., Loboda, T., Sung, S.-J.S., and Black, C.C. (1992). Sucrose synthase in wild tomato *Lycopersicon chmielewskii*, and tomato fruit sink strength. Plant Physiol. **98:** 1163-1169.

Tauzin, A.S., Sulzenbacher, G., Lafond, M., Desseaux, V., Reca, I.B., Perrier, J., Bellincampi, D., Fourquet, P., Lévêque, C., and Giardina, T. (2013). functional characterization of a vacuolar invertase from *Solanum lycopersicum* : post-translational regulation by N-glycosylation and a proteinaceaous inhibitor. Biochimie **101:** 39-49.

Thomas, S., Mooney, P.J., Burrel, M.M., and Fell, D.A. (1997). Metabolic control analysis of glycolysis in tuber tissue of potato (*Solanum tuberosum*). Explanation for the low control coefficient of phosphofructokinase over respiratory flux. Biochem. J. **322:** 119-127.

Tohge, T., Ramos, M.S., Nunes-Nesi, A., Mutwil, M., Giavalisco, P., Steinhauser, D., Schellenberg, M., Willmitzer, L., Persson, S., Martinoia, E., and Fernie, A.R. (2011). Towards the storage metabolome: profiling the barley vacuole. Plant Physiol. **157:** 1469-1482.

Uys, L., Botha, F.C., Hofmeyr, J.H.S., and Rohwer, J.M. (2007). Kinetic model of sucrose accumulation in maturing sugarcane culm tissue. Phytochem. **68:** 2375-2392.

Wang, F., Sanz, A., Brenner M.L, and Smith, A. (1993). Sucrose Synthase, Starch Accumulation,and Tomato Fruit Sink Strength. Plant Physiol. **101:** 321-327.

Wang, L., and Ruan, Y.L. (2010). Unraveling mechanisms of cell expansion linking solute transport, metabolism, plasmodesmtal gating and cell wall dynamics. Plant Signal. Behav. **5:** 1561-1564.

Winter, H., and Huber, S.C. (2000). Regulation of sucrose metabolism in higher plants: localization and regulation of activity of key enzymes. Crit. Rev. Biochem. Mol. Biol. **35:** 253-289.

Yelle, S., Hewitt, J.D., Robinson, N.L., Damon, S., and Bennett, A.B. (1988). Sink metabolism in tomato fruit III. Analysis of carbohydrate assimilation in a wild species. Plant Physiol. **87:** 737-740.

Yelle, S., Chetelat, R.T., Dorais, M., DeVerna, J.W., and Bennett, A.B. (1991). Sink metabolism in tomato fruit IV. Genetic and biochemical analysis of sucrose accumulation. Plant Physiol. **95:** 1026-1035.

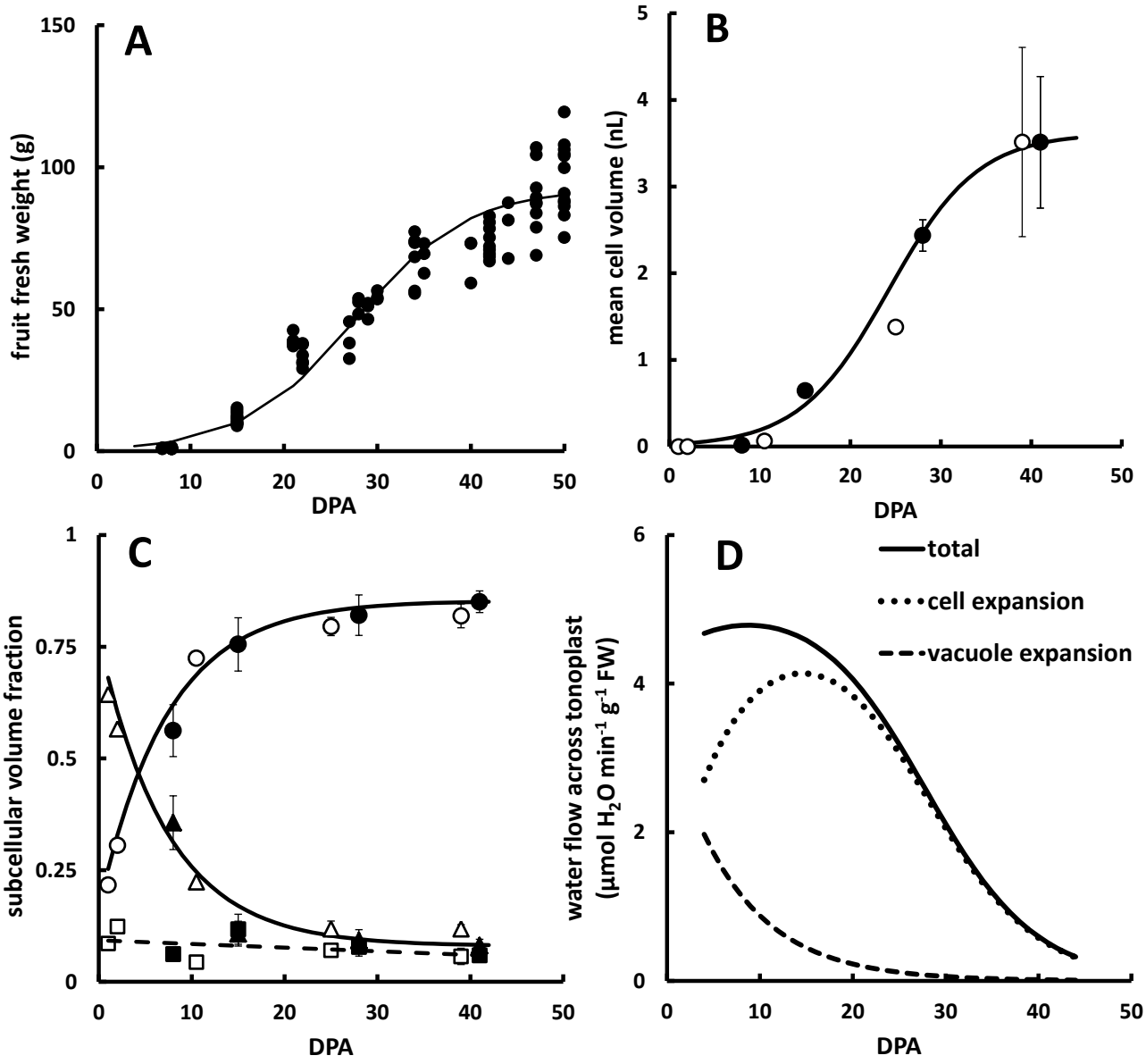

Figure 1. Time-Course Evolution of the Fresh Weight and the Cellular and Subcellular Volumes throughout Fruit Development.

(A) Growth curve of Moneymaker tomato fruit. Continuous line represents the regression analysis using a three-parameter logistic function. **(B)** Mean volume of parenchyma cells of Moneymaker (closed circles) and Ailsa Craig (opened circles) pericarp (mean ± S.D. with n = 3 fruits). **(C)** Fractional volume of vacuole (circles), cytoplasm (triangles) and cell wall (squares) within cells of Moneymaker (closed symbols) and Ailsa Craig (opened symbols) tomato pericarp (mean ± S.D. with n = 3 fruits). Continuous lines represent the non-linear regression of the vacuole and cytoplasm volume fractions and dashed line, that of the cell wall (see supplemental Table 1 for details). **(D)** Water flow across tonoplast resulting from vacuole expansion within cell (dashed line), cell expansion within fruit (dotted line) or both (continuous line).

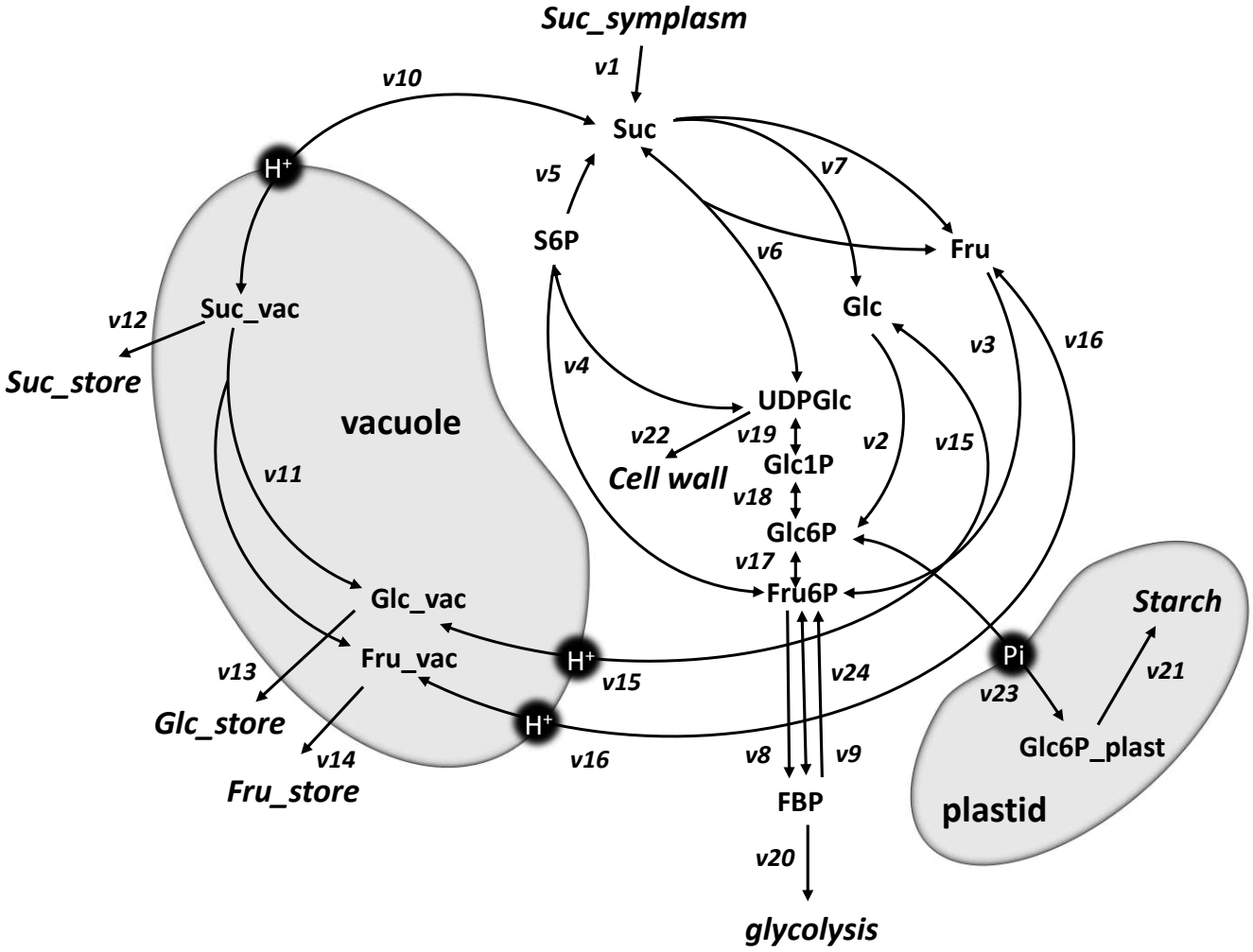

Figure 2. Schematic Network of the Metabolism and Compartmentation of Carbohydrates in Tomato Fruit Pericarp.

Network reactions: v1, sucrose import; v2, glucokinase (GK) ; v3, fructokinase (FK); v4, sucrose-6-P synthase (SPS) ; v5, sucrose-6-phosphatase (SPase); v6, sucrose synthase (Susy); v7, neutral invertase (NI); v8 and v9, ATP- and PPi-dependent phosphofructokinase (PFK and PFP, respectively); v10, sucrose carrier; v11, acid invertase (AI); v12, sucrose storage; v13, glucose storage; v14, fructose storage; v15 and v16, hexose carrier; v17, phosphoglucose isomerase (PGI); v18, phosphoglucomutase (PGM); v19, UDP-glucopyrophosphorylase (UGPase); v20, aldolase (ALD); v21, starch synthesis; v22, cell wall synthesis; v23, glucose-6-P / Pi translocase; v24, fructose-1,6 *bis* phosphatase (FBPase). Output fluxes are italicized. Chemical reactions, rate equations and kinetic parameters are detailed in supplemental Tables 3 and 4.

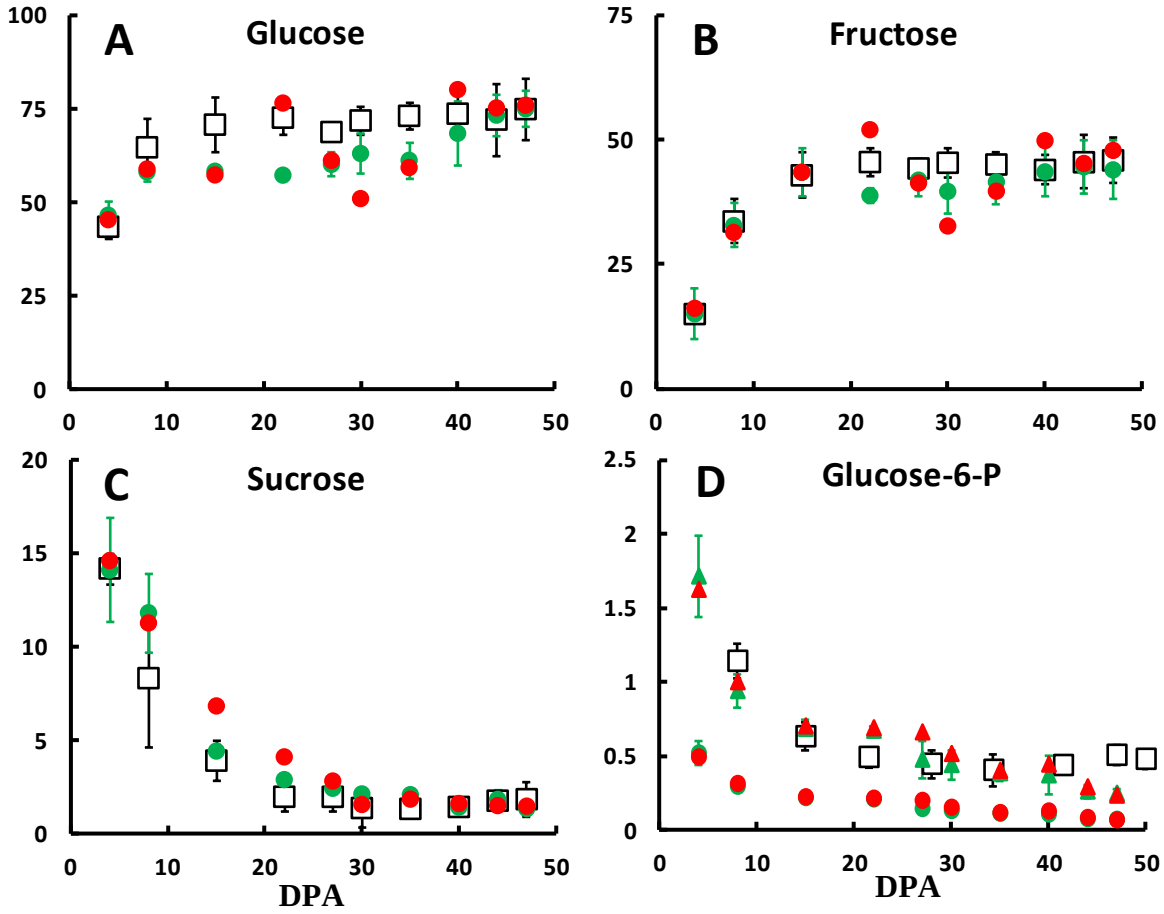

Figure 3. Comparison between Simulated and Experimentally Measured Soluble Sugars and Glucose-6P Contents of Pericarp.

Opened squares represent the pericarp content (in µmol min^{-1} g^{-1} FW, mean ± S.D., n = 3 fruits) of glucose **(A)**, fructose **(B)**, sucrose **(C)** and glucose-6P **(D)** from Biais et al. (2014). At each developmental stage, parameter optimization (V1, $V_{max}10$ and $V_{max}15$ = $V_{max}16$) was carried out as described in Methods. The steady state concentrations of Glc, Fru, Suc and Glc-6P contents were calculated for each parameter combination (n = 300 to 400 parameter sets depending on the stage) and their means ± S.D. were represented by green symbols. Alternately, a new set of parameters was built from the median values of the 300 to 400 combinations and the model run with this new set of parameters gives the calculated Glc, Fru, Suc and Glc-6P contents represented by red symbols. For glucose-6P **(D)**, calculations were performed using a plastid-to-cytoplasm Pi concentration ratio of either 1 (circles) or 20 (triangles).

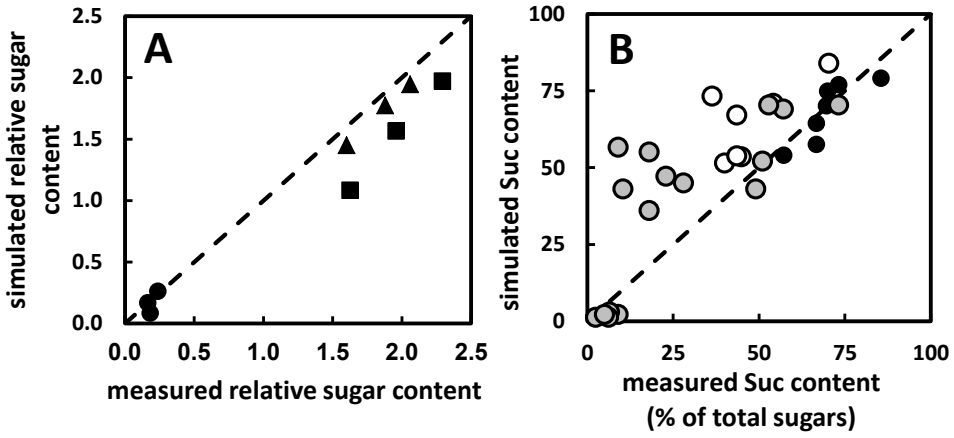

Figure 4. Intra- and Interspecies Cross-Validation of the Model.

(A) Model was parameterized using the enzyme capacities measured with Moneymaker pericarp sampled at 35, 42 and 49 DPA (Steinhauser et al., 2010). Sucrose, glucose and fructose contents (●, ■ and ▲, respectively) are expressed relatively to the 7-DPA aged fruit as in Carrari et al. (2006). **(B)** Model was parameterized using the enzyme capacities measured at breaker stage on ten transgenic lines of *L. esculentum* under-expressing acid invertase (Klann et al., 1996) (grey circles) and at seven developmental stages of the *L. chmielewskii* wild tomato and its introgression lines (Yelle et al., 1988 and 1991) (white and black circles, respectively). Sucrose (Suc) content is expressed as the percentage of total sugars, as in Klann et al. (1996). Diagonals represent the 100% match between simulations and experiments.

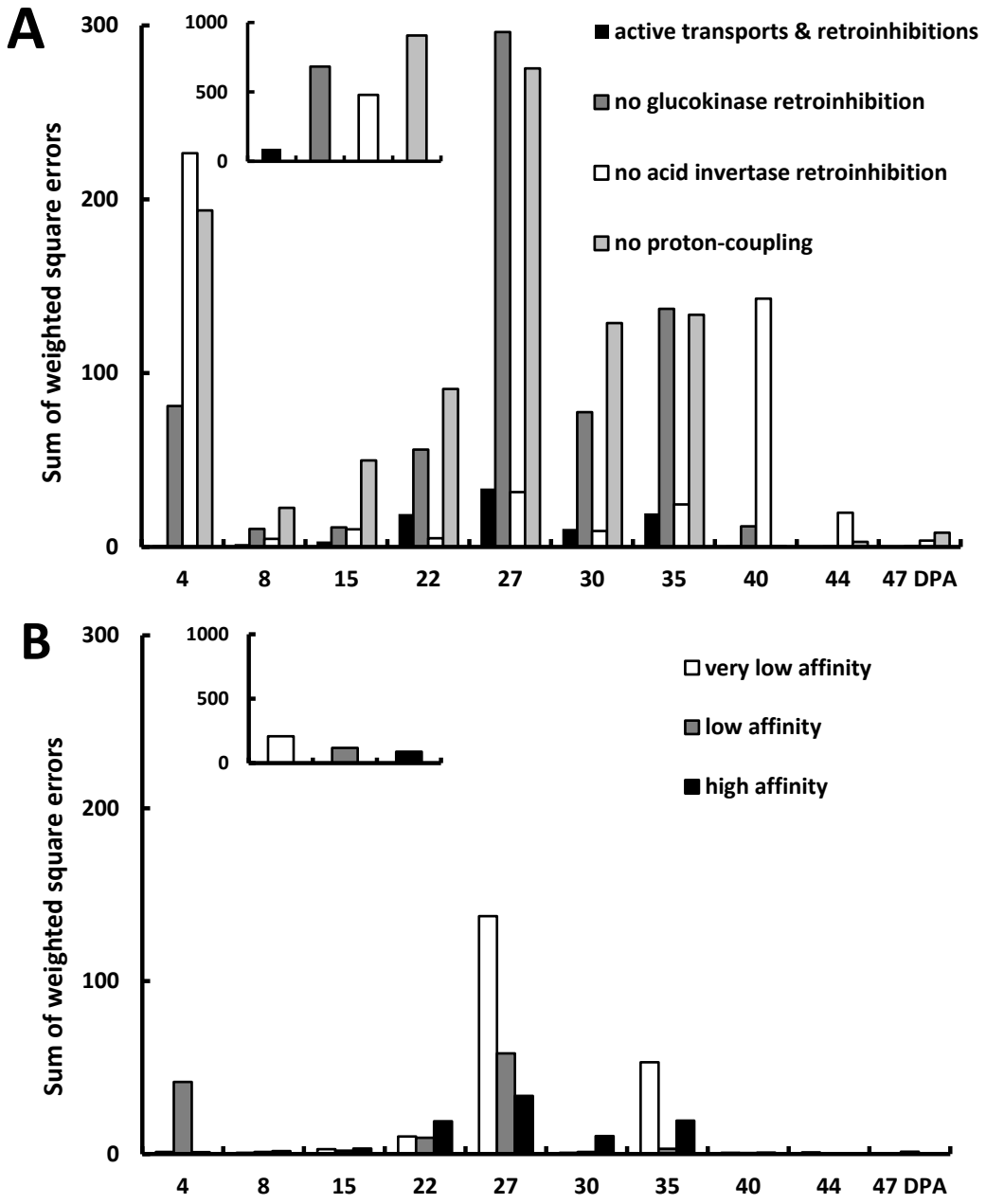

Figure 5. Influence of the Parameterization of the Vacuolar Acid Invertase, Glucokinase and Vacuolar Carriers on the Model Fitness.

(A) Model was parameterized with (black bars) or without the retro-inhibition of glucokinase (dark grey bars) and acid invertase (white bars) or without the H^+-coupling of vacuolar carriers (light grey bars). **(B)** Model was parameterized with a K_m value of the hexose carrier equal to either 40, 4 or 0.4 mM, and that of the sucrose carrier, to either 120, 12 or 1.2 mM, corresponding to very low (white bars), low (grey bars) and high (black bars) affinity conditions, respectively. At each developmental stage and for each condition, parameter optimization (V1, $V_{max}10$ and $V_{max}15 = V_{max}16$) was carried out and the sum of squared residuals between measurements and calculations of Glc, Fru and Suc (see supplemental Figure 6 for raw results), weighted by the standard deviation of each measurement, was calculated to score the model fitness. Inserts show the cumulative sum of squared residuals over all stages.

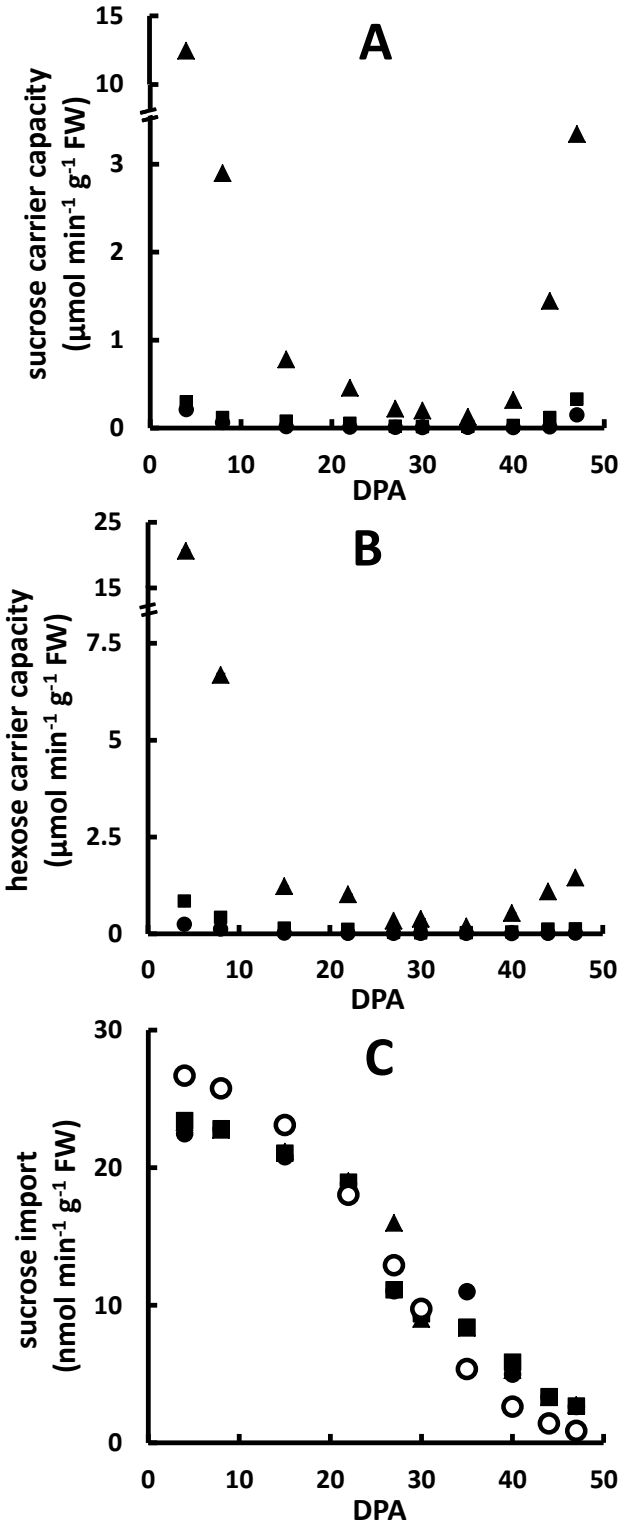

Figure 6. Model Predictions of the Capacity of Vacuolar Carriers and the Sucrose Import of Pericarp Cells.

At each developmental stage, parameter optimization (V1, $V_{max}10$ and $V_{max}15 = V_{max}16$) was carried out for three different models parameterized using either a very low (triangles), low (circles) or high (squares) affinity of the vacuolar carriers, as in Figure 5B. The plotted values are the median (n = 300 to 400 parameter sets) of the respective parameters and come from the boxplot graphs of supplemental Figure 7. **(A)** V_{max} of the sucrose carrier ($V_{max}10$). **(B)** V_{max} of the hexose carrier ($V_{max}15 = V_{max}16$). **(C)** Sucrose import (V1). Opened circles represent values predicted by the fruit construction cost model of Heuvelink (1995).

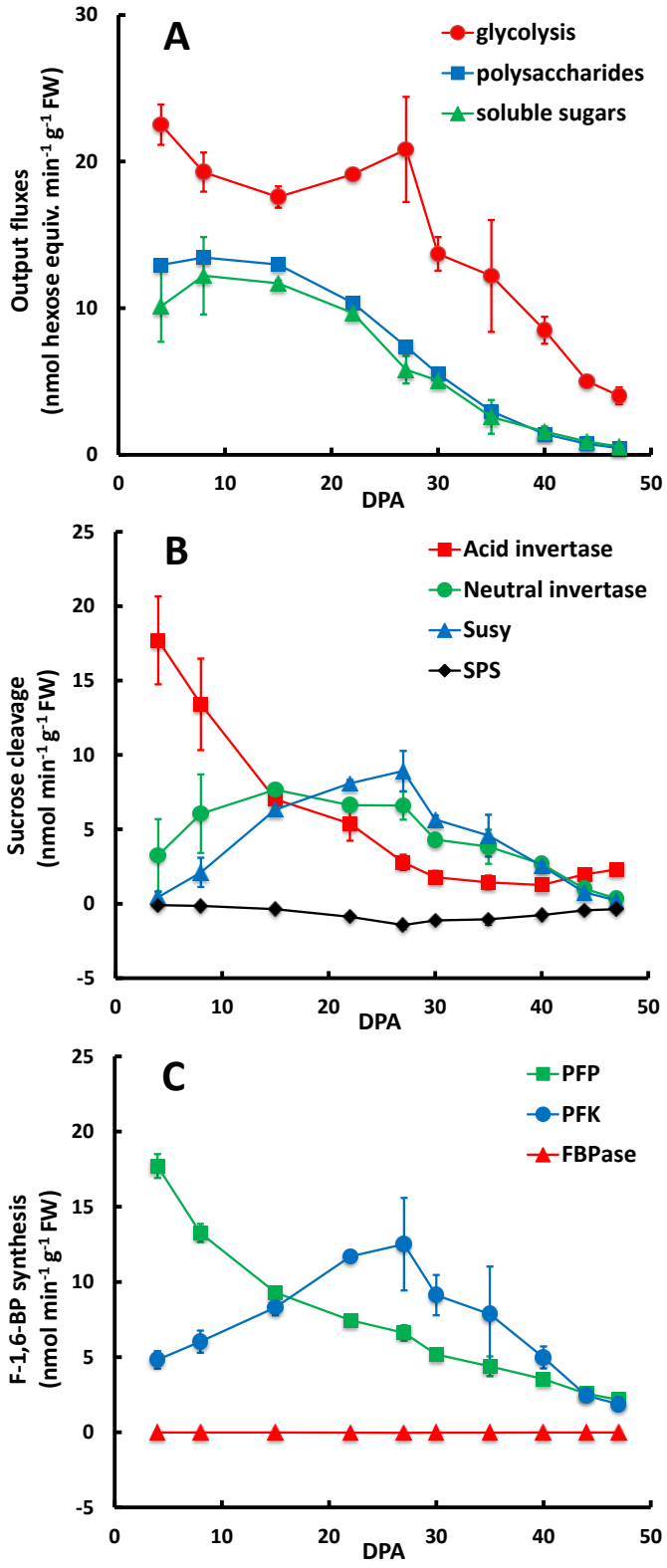

Figure 7. Flux Partitioning within the Network during Fruit Growth.

At each developmental stage, fluxes were calculated at steady state using the optimized parameters (V1, $V_{max}10$ and $V_{max}15$ = $V_{max}16$) of Figure 6. Values are means ± S.D. of fluxes calculated under conditions of very low, low and high affinity vacuolar carriers. **(A)** Output fluxes of polysaccharide synthesis (V21+V22) (■), sugar storage (V12*2+V13+V14) (▲) and glycolysis (V20) (●). **(B)** Fluxes of the sucrose cycle enzymes, i.e. acid- (V11) (■) and neutral invertase (V7) (●), Susy (V6) (▲) and SPS (V4) (♦). **(C)** Fluxes of the Fru-1,6-*bis*-P cycle enzymes, i.e. PFP (V9) (■), PFK (V8) (●) and FBPase (V24) (▲). Note that the flux values of SPS and FBPase are negative. Abbreviations are the same as in Figure 2.

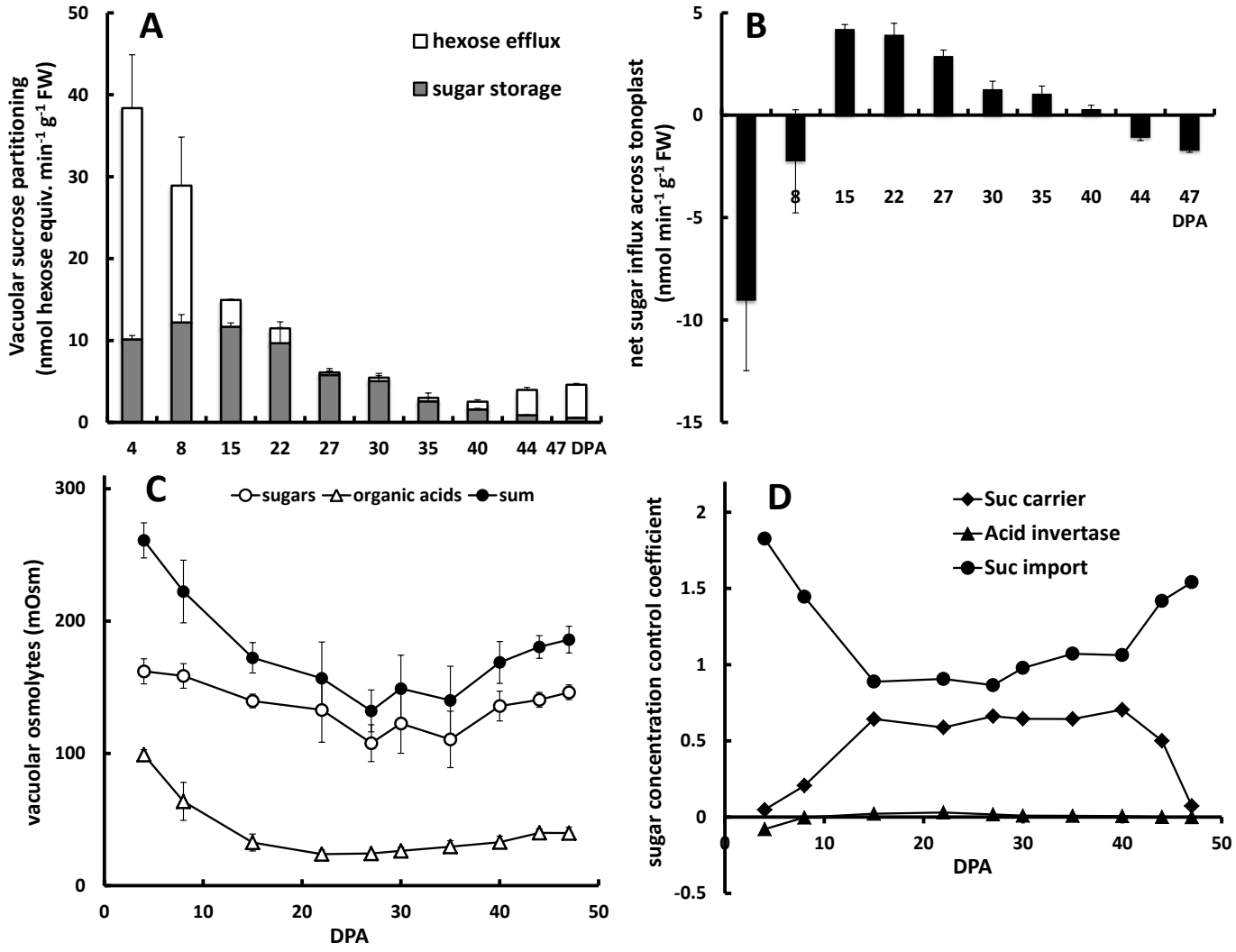

Figure 8. Role of Sugars and Organic Acids in the Osmotic Strength of the Vacuole during Fruit Growth.

At each developmental stage, fluxes and concentrations were calculated at steady state using the optimized parameters (V1, $V_{max}10$ and $V_{max}15$ = $V_{max}16$) of Figure 6. Values are means ± S.D. of values calculated under conditions of very low, low and high affinity vacuolar carriers. **(A)** Partitioning of the sucrose transported into the vacuole between sugar storage (V12*2+V13+V14) and hexose efflux (V15+V16) (grey and white bars, respectively). **(B)** Net sugar influx across the tonoplast (V10+V15+V16). **(C)** Contribution of sugars (○), organic acids (Δ) and both (●) to the osmotic strength of the vacuole. **(D)** Control of the concentration of sugars in the vacuole by the acid invertase (▲), the vacuolar sucrose carrier (♦) and the cellular sucrose import (●).

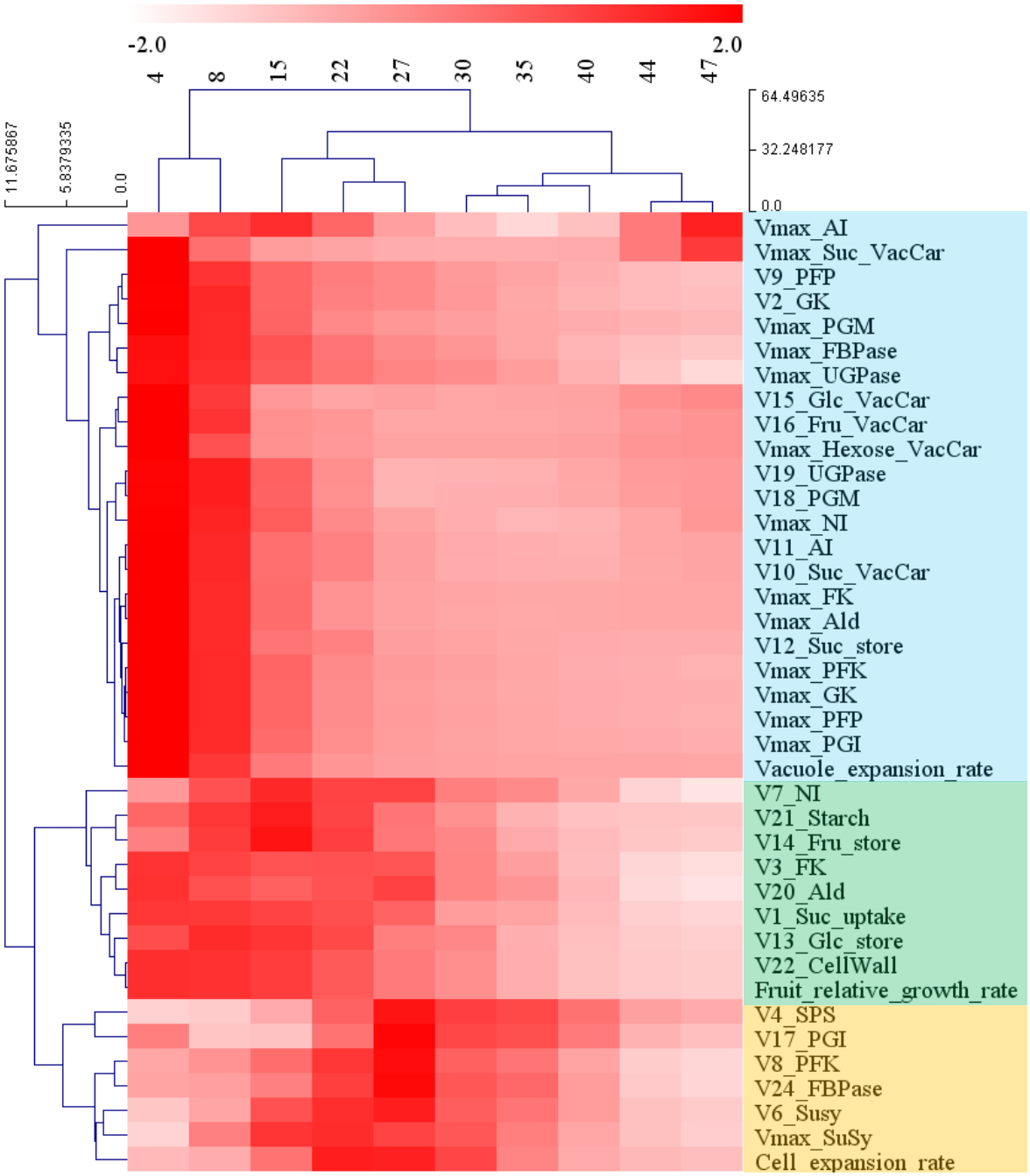

Figure 9. Hierarchical Clustering of Fluxes and Enzyme Capacities together during Fruit Growth.

Heat map was obtained after two-dimension Hierarchical Clustering Analysis, where columns correspond to the ten developmental stages and rows to mean-centered scaled to unit variance fluxes and enzyme capacities. Three main clusters were highlighted corresponding to the coloured bars on the right. Colour code: Blue, higher values during cell division; Green, higher values during cell division and beginning of cell expansion; Yellow, higher values at mid expansion. Abbreviations are the same as in Figure 2.

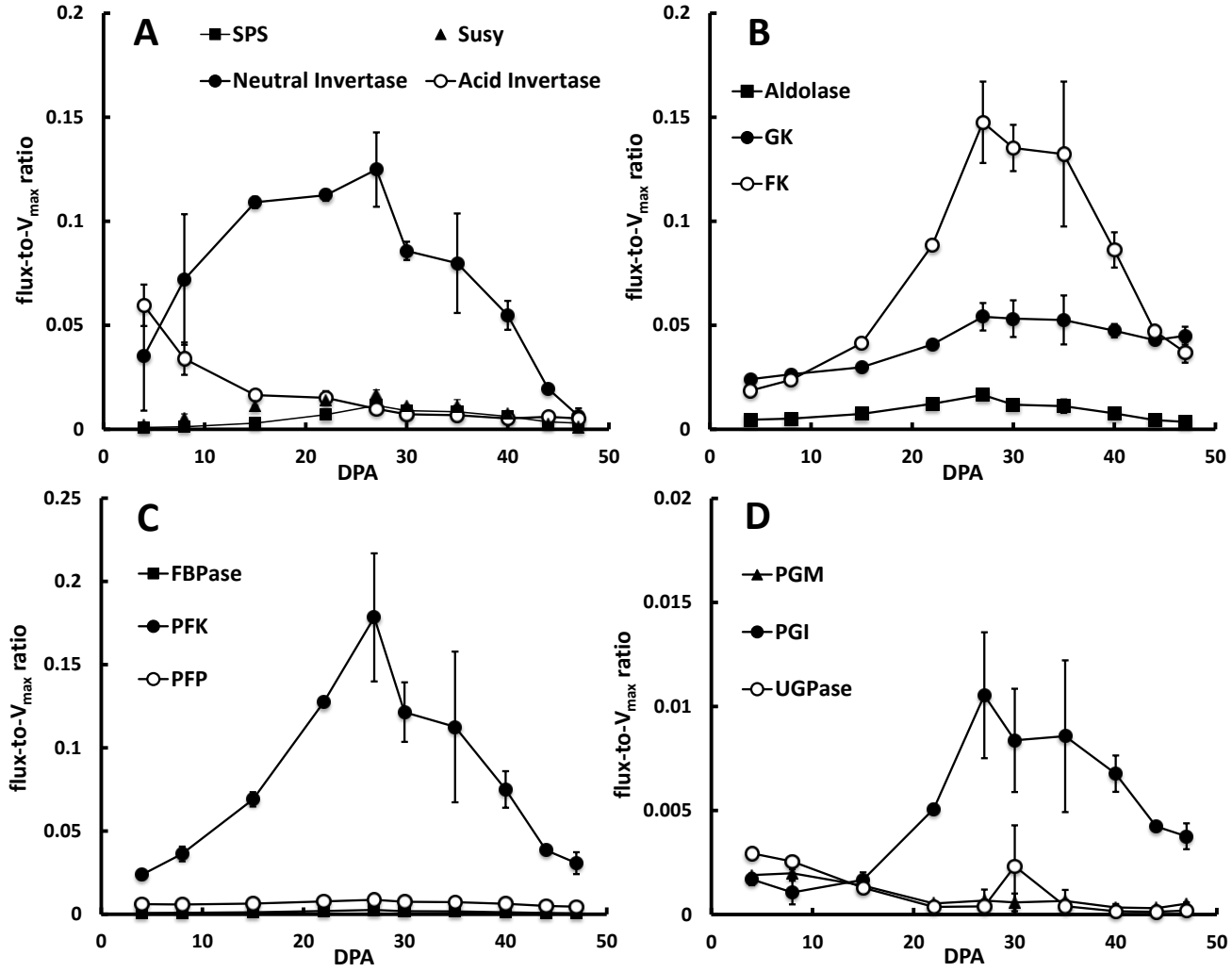

Figure 10. Fractional Velocity of Enzymes during Fruit Growth.

Fractional velocity, *i.e.* flux-to-V_{max} ratio, was calculated from the flux and V_{max} values of the respective enzymes. Values are means ± S.D. of fluxes calculated under conditions of very low, low and high affinity vacuolar carriers. **(A)** Enzymes of the sucrose cycle. **(B)** Aldolase, gluco- and fructokinase. **(C)** Enzymes of the Fru-1,6BP cycle. **(D)** Hexose-P interconverting enzymes. Abbreviations are the same as in Figure 2.

SUPPLEMENTAL DATA

Model-assisted analysis of sugar metabolism throughout tomato fruit development reveals enzyme and carrier properties in relation to vacuole expansion

Bertrand Beauvoit[a,b,1], Sophie Colombié[a], Antoine Monier[a], Marie-Hélène Andrieu[a], Benoit Biais[a], Camille Bénard[a], Catherine Chéniclet[a,b,c,d,e], Martine Dieuaide-Noubhani[a,b], Christine Nazaret[f], Jean-Pierre Mazat[b,g], Yves Gibon[a]

[a] INRA, UMR 1332 Biologie du Fruit et Pathology, F33883 Villenave d'Ornon Cedex, France

[b] Univ. Bordeaux, 146 rue Léo-Saignat, F-33076 Bordeaux Cedex, France.

[c] Univ. Bordeaux, Bordeaux Imaging Center, UMS 3420, F-33000 Bordeaux, France

[d] CNRS, Bordeaux Imaging Center, UMS 3420, F-33000 Bordeaux, France

[e] INSERM, Bordeaux Imaging Center, US 004, F-33000 Bordeaux, France

[f] Institut de Mathématiques de Bordeaux, ENSTBB-Institut Polytechnique de Bordeaux, F-33600 Pessac, France

[g] IBGC-CNRS, UMR 5095, 1 rue Camille Saint-Saëns, 33077 Bordeaux cedex, France

Corresponding author:

Bertrand Beauvoit

INRA, UMR 1332 Biologie du Fruit et Pathologie

F-33883 Villenave d'Ornon Cedex

France

Tel: +33 557 122 651

Email: bbeauvoi@bordeaux.inra.fr

Supplemental Figure 1. Time courses of enzyme capacities and polysaccharide contents throughout fruit growth.

Maximal activity of enzymes (V_{max}), expressed as in µmol of substrate or product consumed or synthesized g^{-1} Fresh Weight (FW), cell wall and starch contents, expressed as in µmol of glucose equivalent g^{-1} FW, were measured at different developmental stages (Biais et al., 2014). Time post anthesis is expressed in min. The corresponding cubic polynomial parameters of the best fit are listed in supplemental Table 2.

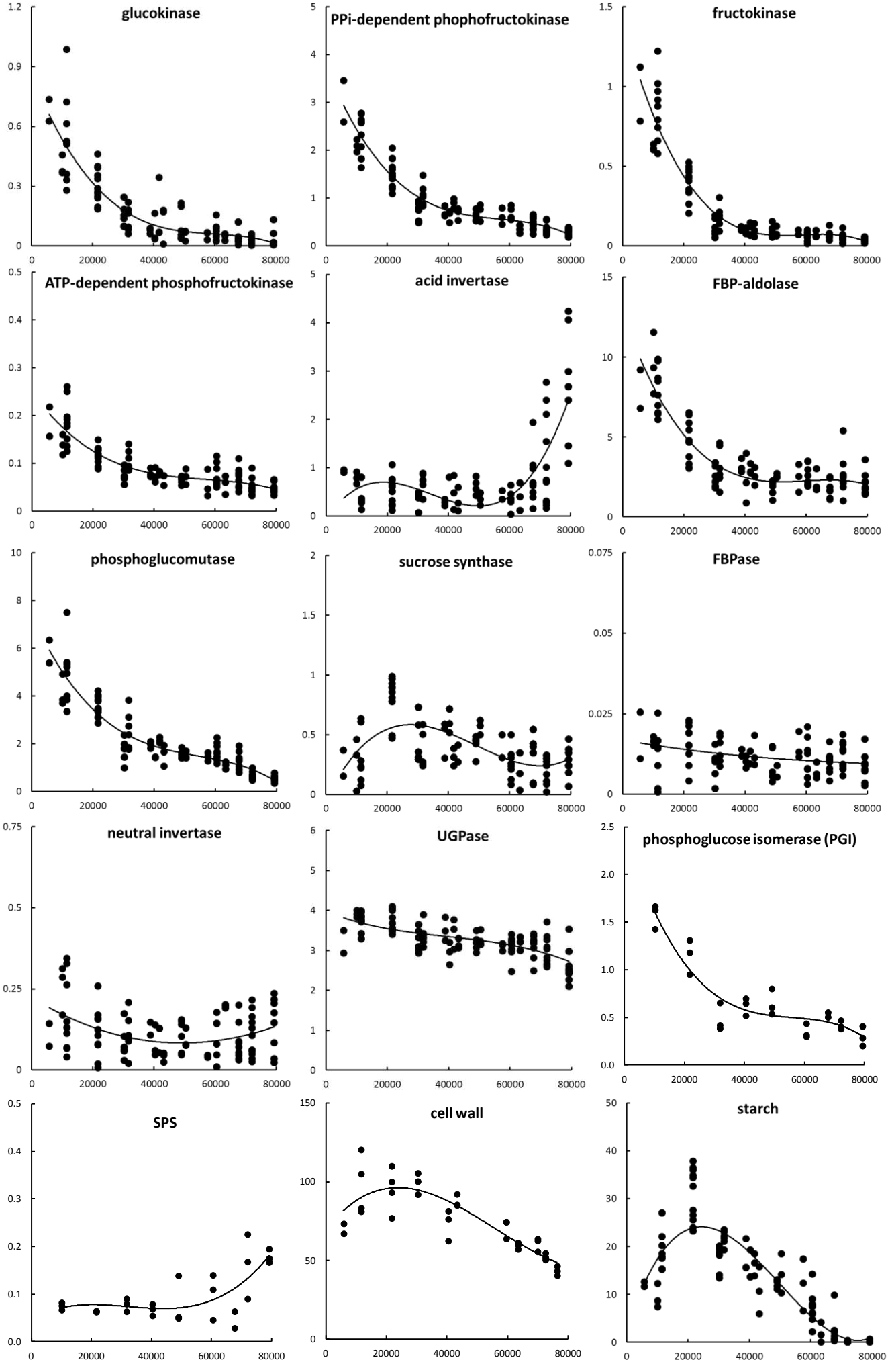
glucokinase
PPi-dependent phophofructokinase
fructokinase
ATP-dependent phosphofructokinase
acid invertase
FBP-aldolase
phosphoglucomutase
sucrose synthase
FBPase
neutral invertase
UGPase
phosphoglucose isomerase (PGI)
SPS
cell wall
starch

Supplemental Figure 2. Estimation of the vacuolar pH throughout fruit growth.

(A) Vacuolar pH, measured *in vivo* by ^{13}C NMR on cherry tomato, as a function of the total content of malate *plus* citrate (expressed in µmol g^{-1} dry weight) adapted from Rolin et al. (2000). Linear regression analysis gave the following equation: $y = -2.04\ 10^{-3} * x + 5.133$ ($R^2 = 0.84$).

(B) Malate *plus* citrate content of Moneymaker pericarp as a function of developmental stage (from Biais et al., 2014).

(C) Vacuolar pH of Moneymaker pericarp, calculated from the above equation and the measured malate *plus* citrate content, as a function of the developmental stage. Taking a cytosolic pH value of 7.1 (Rolin et al., 2000), the averaged vacuolar ΔpH throughout fruit development is equal to 2.92 ± 0.27.

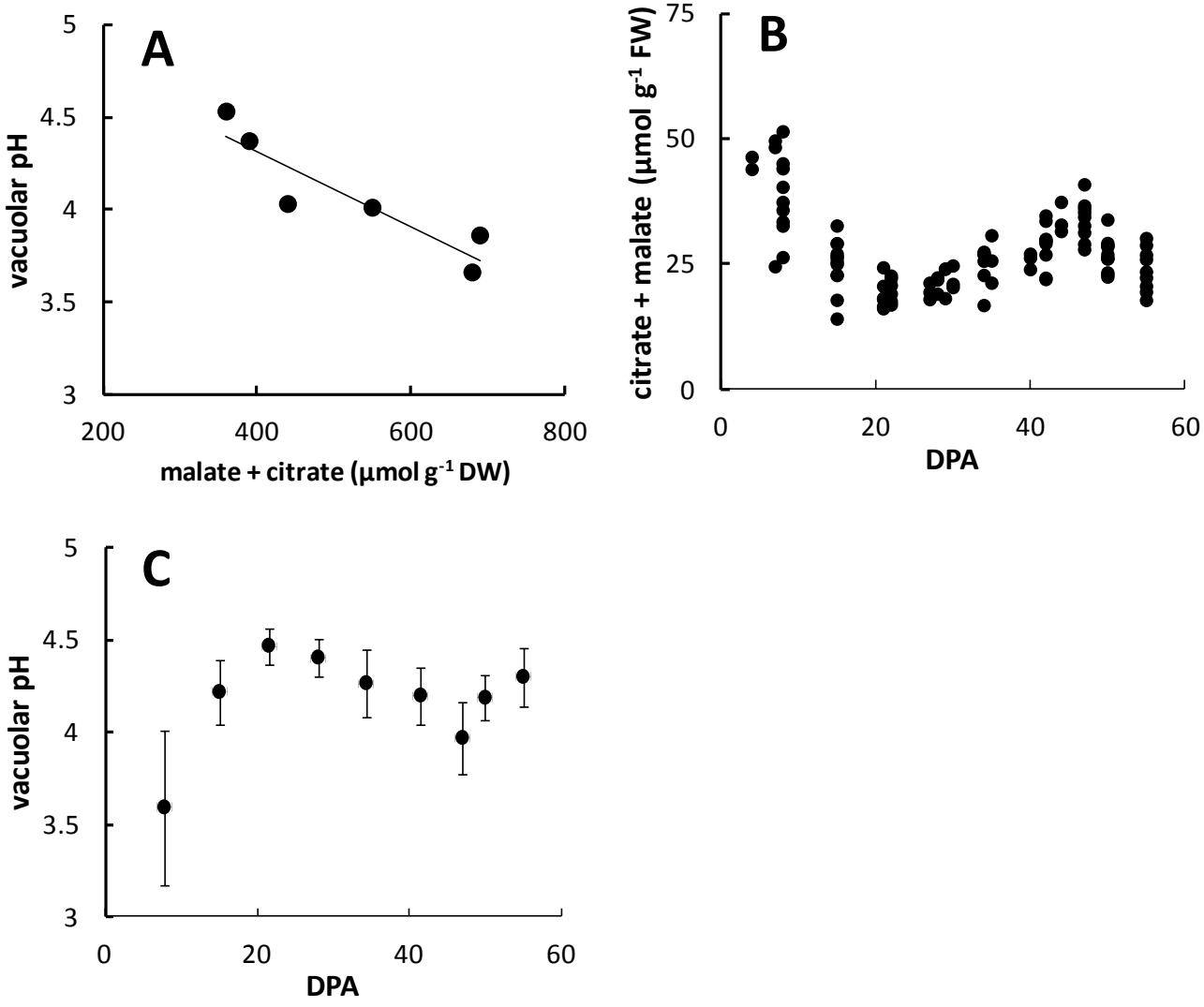

Supplemental Figure 3. Time courses of the adenylic nucleotides and phosphate content of pericarp tissue throughout fruit growth.

ATP, ADP and Pi contents of fruit pericarp were measured on perchloric acid extracts using bioluminescence and colorimetric assays, as described in Methods.

(A) Total ATP and ADP contents of pericarp tissue (mean ± S.D. with n = 3 fruits). Continuous lines represent the cubic polynomial regression analysis (R^2 = 0.94 and 0.59, respectively).

(B) Cytoplasmic ATP and ADP concentrations, calculated using the curve fit equations of panel A and the time course of the cytoplasmic volume of Figure 1C.

(C) ATP-to-ADP ratio, calculated from the data of panel A. Continuous line represents the ratio calculated from the curve fit equations of panel A. Averaged ATP/ADP ratio is equal to 5.3 ± 0.9.

(D) Total Pi content of pericarp tissue. Averaged Pi content throughout the fruit development is equal to 4.6 ± 0.5 µmol g^{-1} FW.

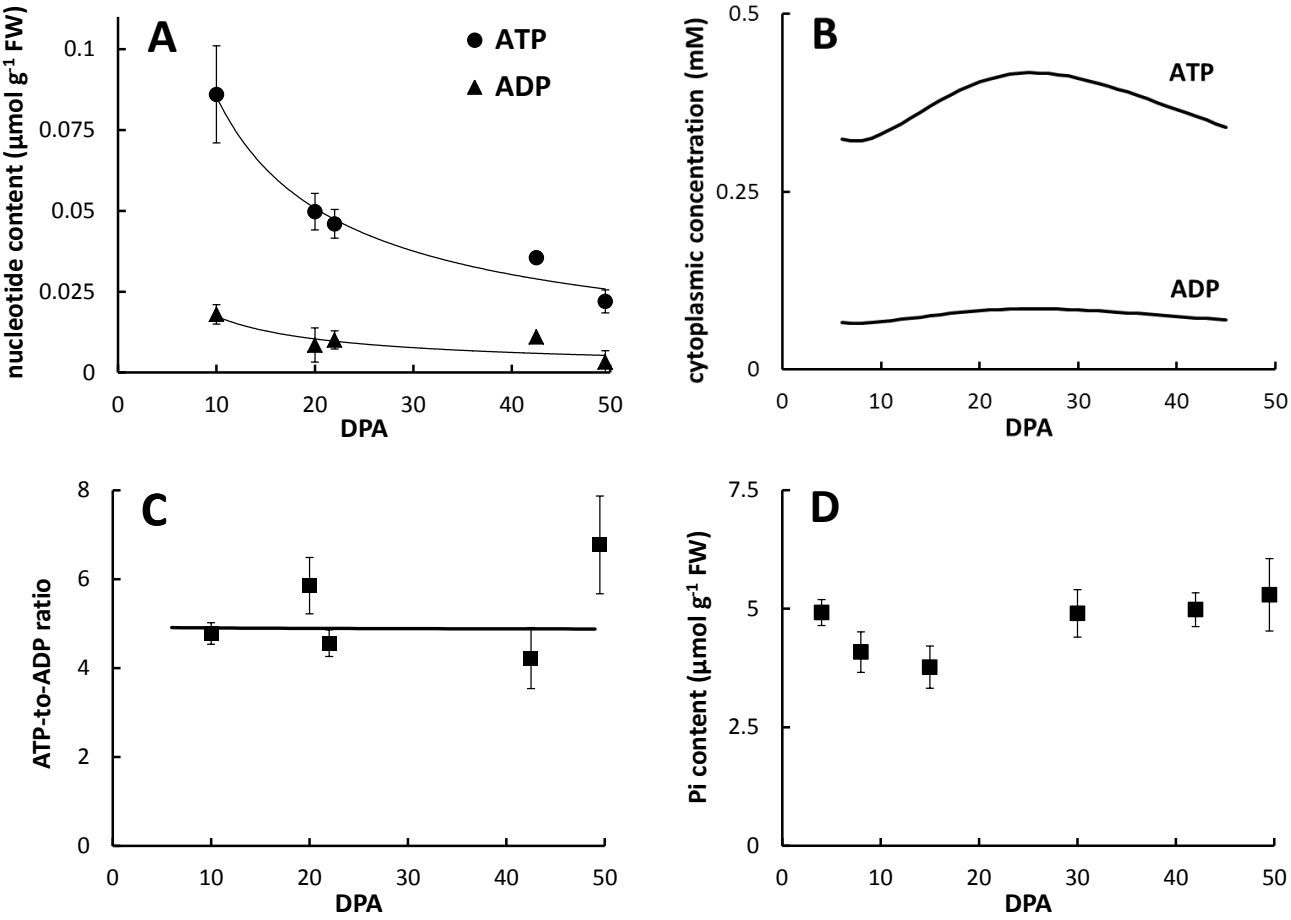

Supplemental Figure 4. Flux variability as a function of developmental stage.

At each developmental stage, parameter optimization (i.e. V1, $V_{max}10$, V_{max} = $V_{max}16$) was performed as described in Methods. For each combination of optimized parameters (n = 300 to 400 parameter sets), fluxes were calculated at steady state. The flux variation coefficient, i.e. the standard deviation-to-mean ratio, was subsequently calculated as an indicator of flux determination accuracy. Abbreviations are the same as in Figure 2.

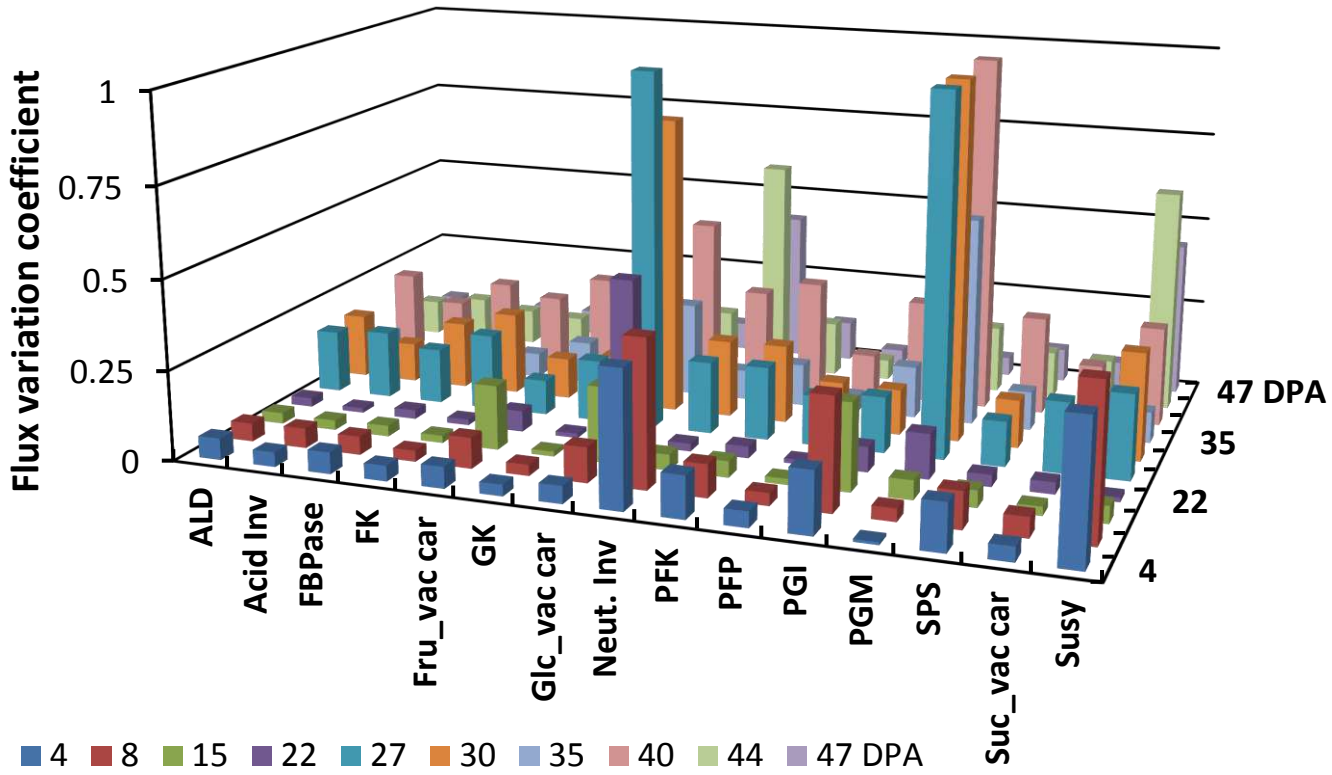

Supplemental Figure 5. Sensitivity coefficients of the calculated glucose, fructose and sucrose content towards the parameterization of glucokinase, acid invertase and vacuolar carriers.

Sensitivity analysis of the model was performed at each developmental stage (in DPA) as described in Methods. The analysed parameters were ΔpH, the affinity constant of vacuolar carriers (i.e. K_m10 and $K_m15 = K_m16$) and the inhibition constants of acid invertase (i.e. K_i11Fru and K_i11Glc) and glucokinase (i.e. K_i2G6P and K_i2F6P). Outputs of the sensitivity analysis were the sucrose (orange circles), glucose (red squares) and fructose (blue triangles) contents.

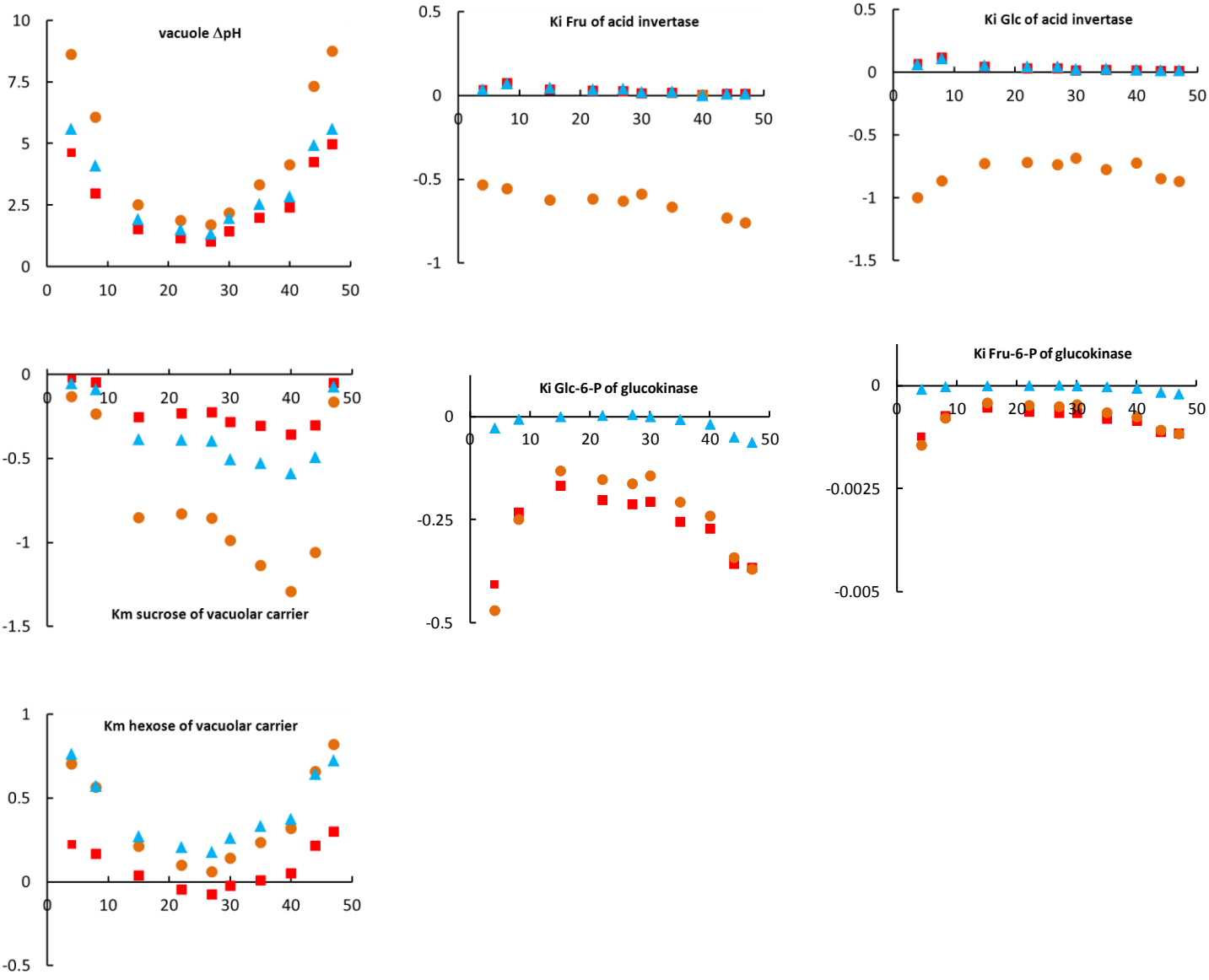

Supplemental Figure 6. Influence of the parameterization of the vacuolar acid invertase, glucokinase and sugar carriers on the model fitness.

At each developmental stage, parameter optimization (*i.e.* V1, $V_{max}10$, $V_{max}15$ = $V_{max}16$) was performed as described in Methods, in the absence of H^+-coupling of the carriers (A, B, C) and in the absence of retroinhibition of acid invertase (D, E, F) or glucokinase (G, H, I). Experimentally measured (closed circles, mean ± S.D. from Biais et al. (2014)) and calculated (opened circles, mean ± S.D. with n = 300 to 400 parameter sets) glucose (A, D, G), fructose (B, E, H) and sucrose (C, F, I) (expressed in µmol g^{-1} FW) are plotted as a function of DPA.

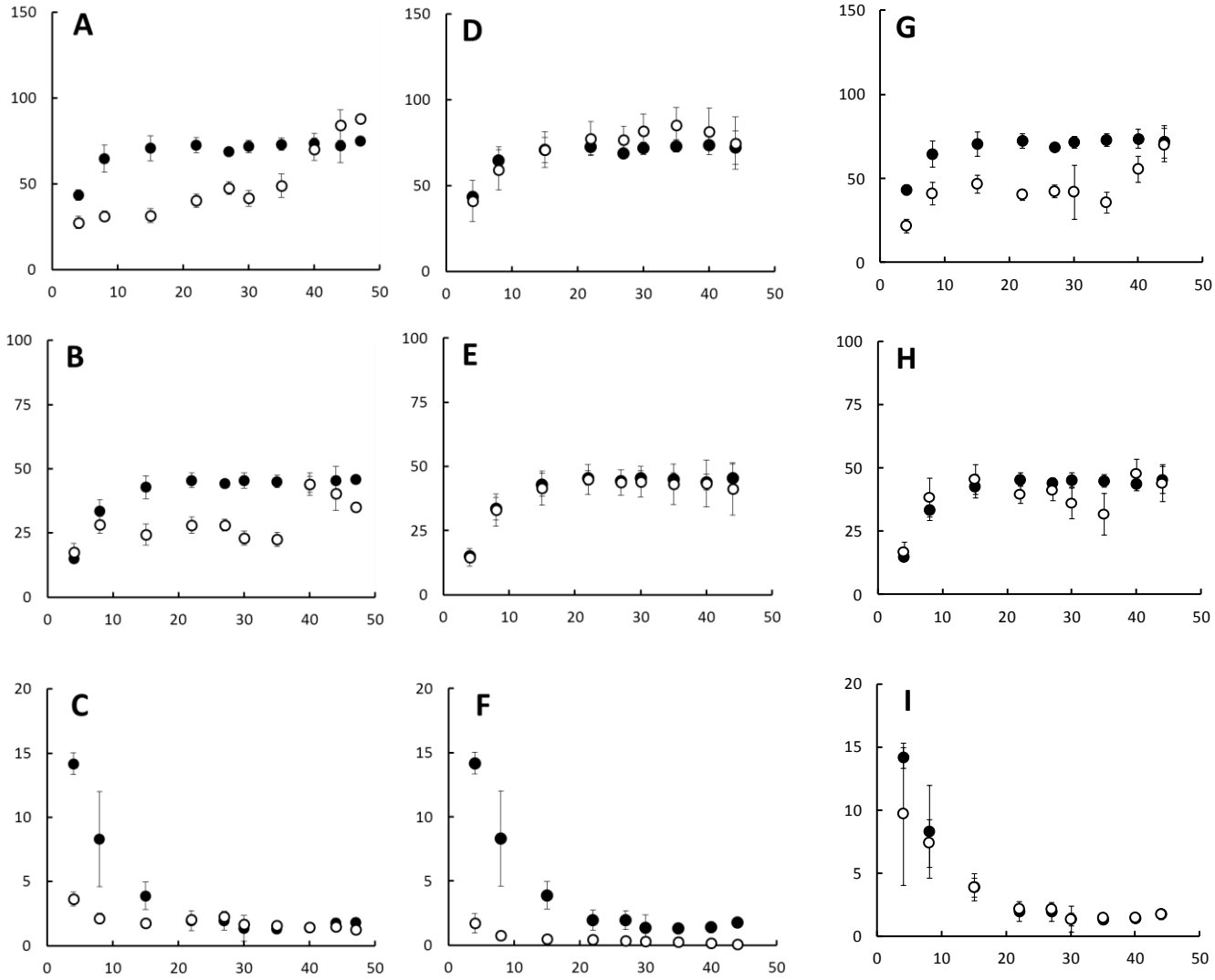

Supplemental Figure 7. Boxplot graphs of optimized values of the vacuolar carrier capacities and sucrose import.

At each developmental stage, parameter optimization (V1, $V_{max}10$ and $V_{max}15$) was carried out under conditions of high (A, B, C), low (D, E, F) and very low (G, H, I) affinity of vacuolar carriers, as described in Figure 5 and in Methods (n =300 to 400 parameter sets).

A, D and G: V_{max} values of the Suc carrier ($V_{max}10$).

B, E and H: V_{max} values of the hexose carrier ($V_{max}15 = V_{max}16$).

C, F and I: Suc import values (V1).

Black circles represent the mean values of each parameter set.

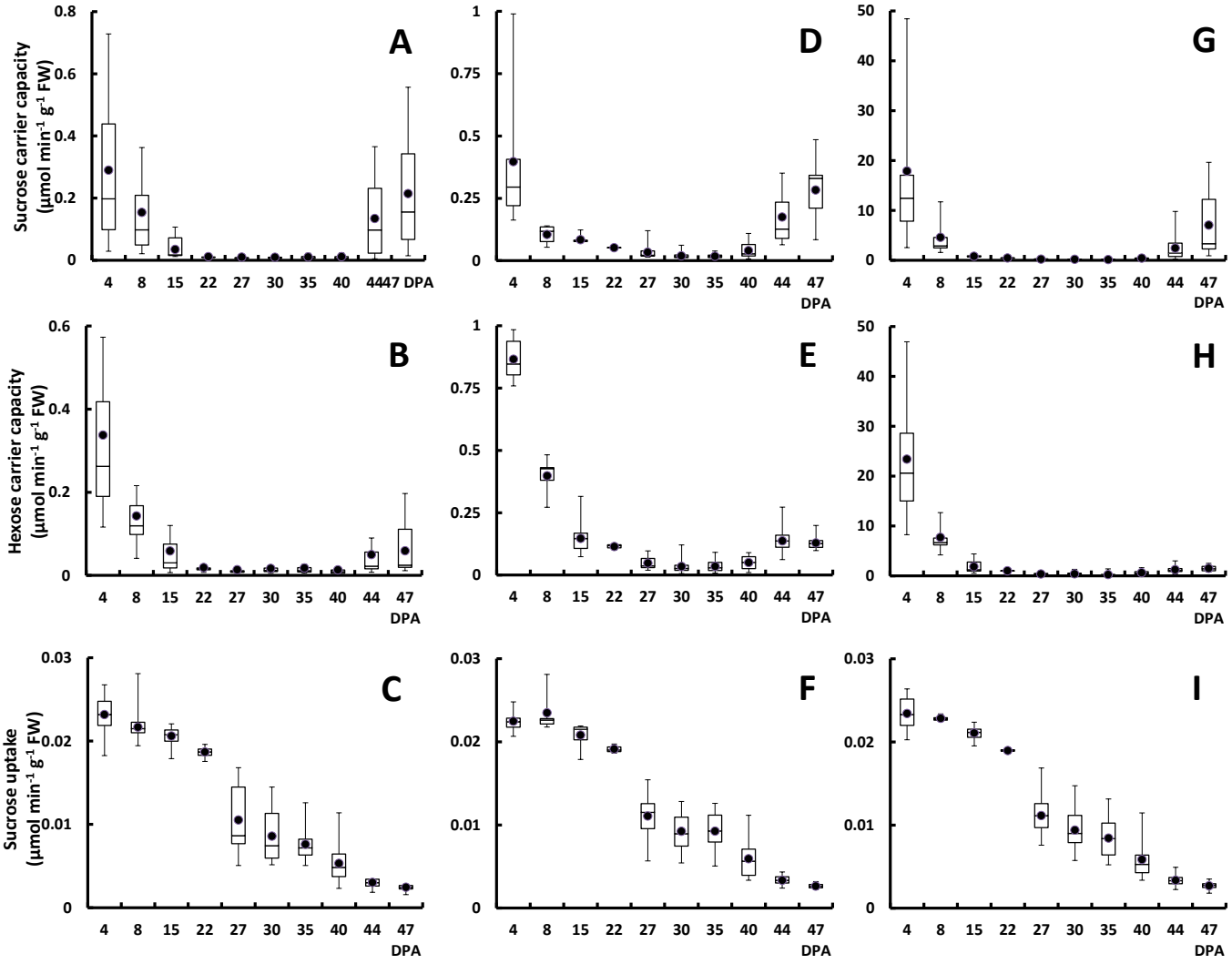

Supplemental Figure 8. Control of the sucrose inter-converting fluxes by enzymes.

The control coefficients of fluxes towards infinitesimal changes in the Susy (orange circles), neutral invertase (red squares), acid invertase (blue triangles), sucrose carrier (green diamonds) and SPS (green dash) activity were calculated at each developmental stage (in DPA), as described in Methods.

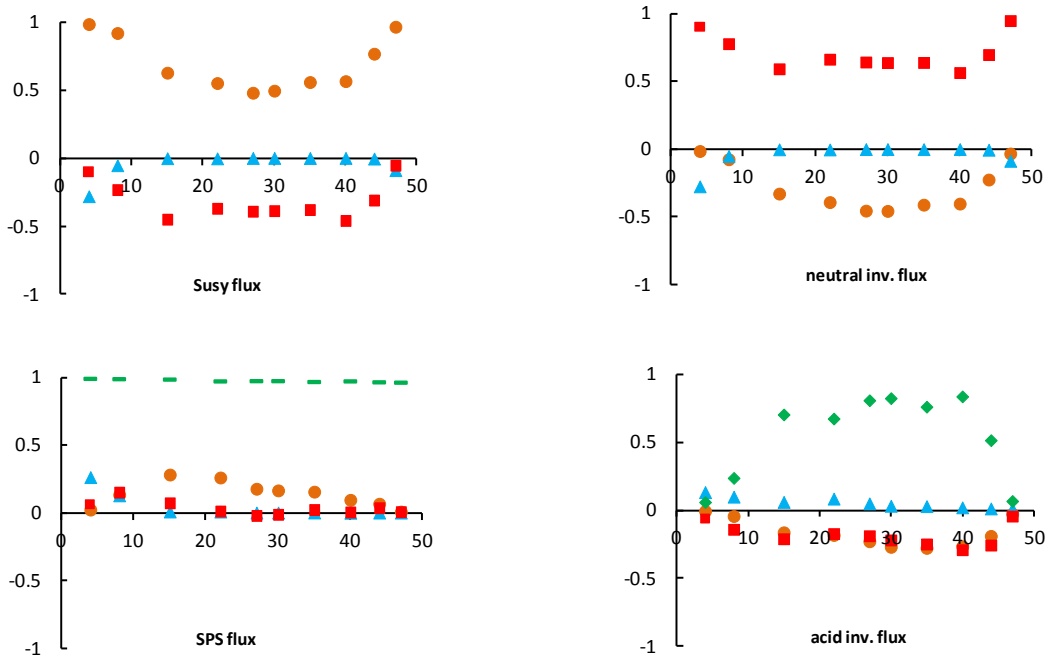

Supplemental Figure 9. Evolution of the concentrations of sugars and organic acids within the vacuole and cytoplasm.

At each developmental stage, sugar concentrations were calculated at steady state using the optimized parameters (V1, $V_{max}10$ and $V_{max}15 = V_{max}16$) of Figure 6. Values are means ± S.D. of concentrations calculated under conditions of very low, low and high affinity vacuolar carriers. Malate and citrate concentrations were calculated at each stage as described in Lobit et al. (2006), using the malate and citrate contents (in µmol g^{-1} FW) from Biais et al. (2014), the pK_a values of malate being equal to 3.4 and 5.1 and those of citrate, to 3.14, 4.77 and 6.39, and the electrical potential and pH differences across tonoplast being equal to 30 mV and 2.94, respectively. (A) and (C), vacuolar concentrations (in mM) and, (B) and (D), cytoplasmic concentrations (in mM).

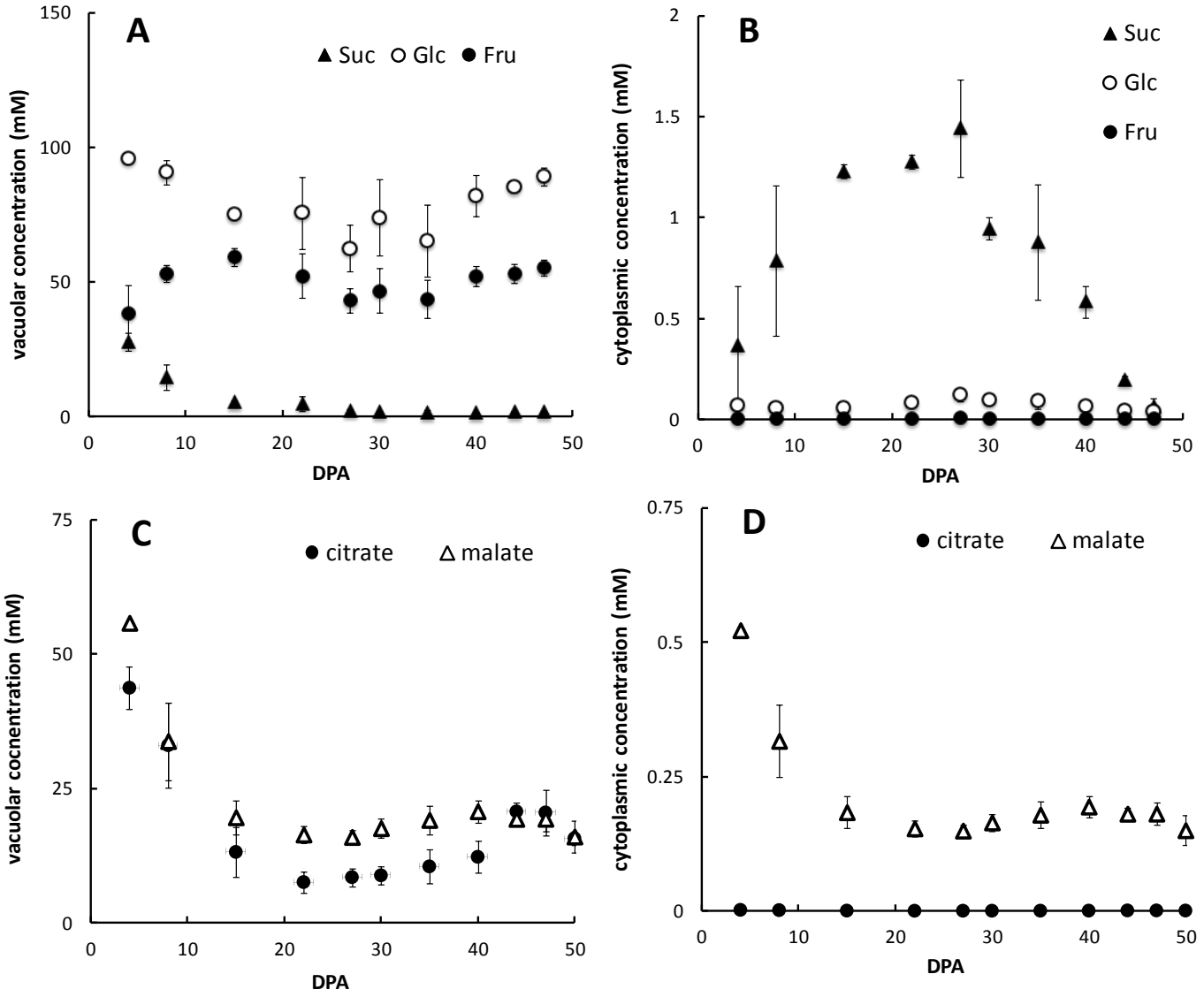

Supplemental Figure 10. Control of the sugar accumulation by enzymes and fruit growth.

The control coefficients of the total soluble sugar content towards infinitesimal changes in enzyme activities were calculated at each developmental stage (in DPA), as described in Methods. Abbreviations are the same as in Figure 2.

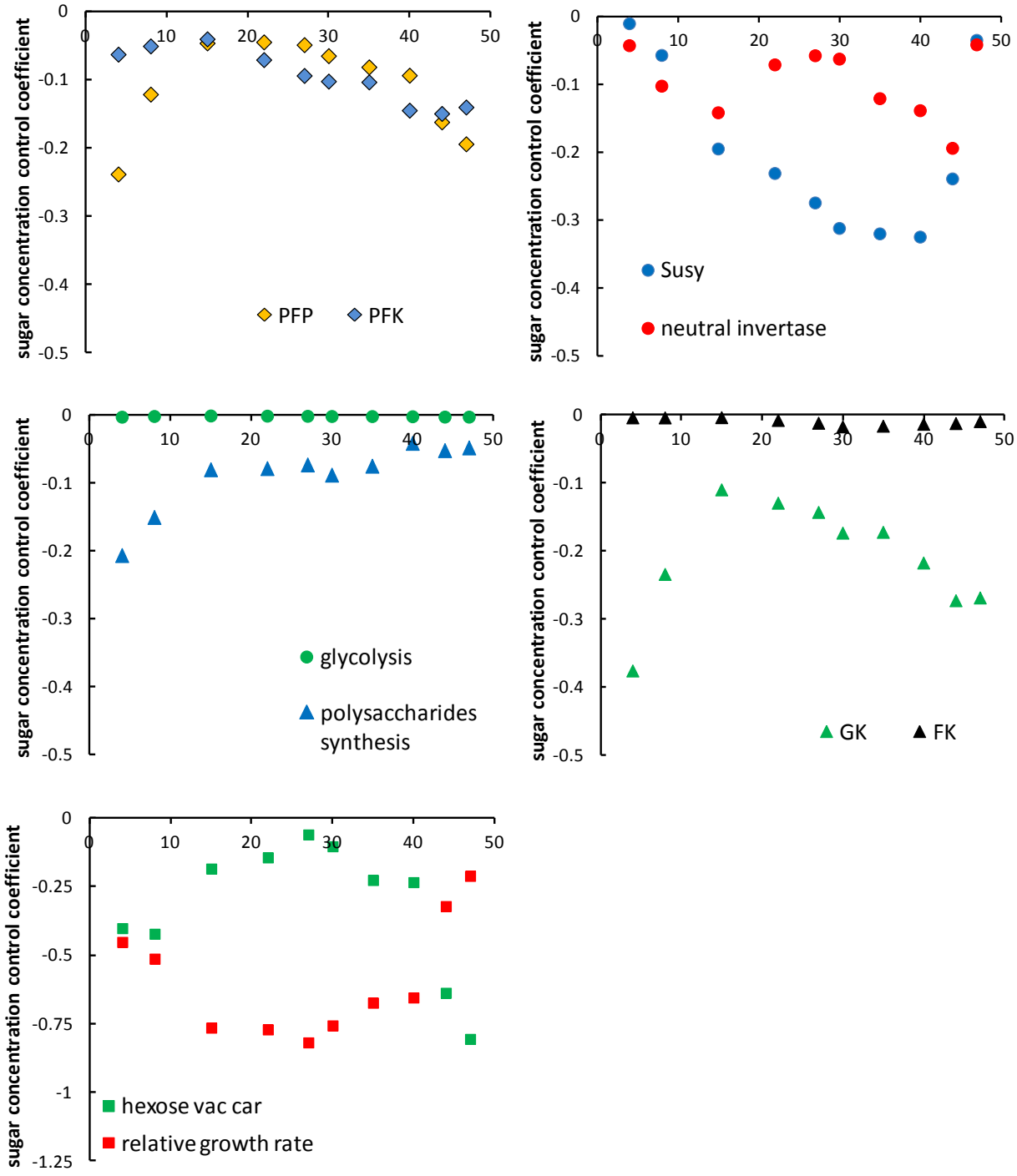

Supplemental Table 1. Nucleotide concentrations, vacuolar ΔpH and compartment volumes of the kinetic model.

Parameter	Constant value or time-dependent function £	R^2	Value range & references
Vacuole volume fraction (V_{vac})	0.853*(1-exp((-2292-Time)/10633))	0.99	Figure 1
Cytoplasm volume fraction (V_{cyt})	0.933 - V_{vac}	-	Figure 1
Plastid volume fraction (V_{plast})	0.13 * V_{cyt}	-	see text
ATP	106.846*Time^(-0.745)	0.94	suppl. Fig. 3, see also [a, b]
UTP	ATP / 3 §	-	[b]
ADP	21.172*Time^(-0.742)	0.59	suppl. Fig. 3, see also [a, b]
UDP	ADP /3 §	-	[b]
Pi	4.6	-	suppl. Fig. 3
Vacuole ΔpH	2.9	-	suppl. Fig. 2
PPi	0.034 $	-	0.012 - 0.2 [c, d]

Footnotes : £ Concentrations are expressed as in µmol g^{-1} FW. During modelling, local concentrations of metabolites were calculated using the respective volume fraction of the compartment(s) and the tissue density *d*. § Assuming an ATP/UTP ratio of about 3, ATP/ADP and UTP/UDP ratio of about 5 in green fruits [Centeno et al. (2011) Malate plays a crucial role in starch metabolism, ripening, and soluble solid content of tomato fruit and affects postharvest softening. Plant Cell 23: 162-184]. $ Parameter optimization (n = 450) performed on several developmental stages (4 to 47 DPA) gives a PPi concentration equal to 0.034 ± 0.014 mM. This value is in the 10 to 50 µM range that can be estimated from previous measurements [Osorio et al. (2013) Pyrophosphate levels strongly influence ascorbate and starch content in tomato fruit. Frontiers in Plant Science, 4: article n°308].

References: [a] Menu et al. (2003) High hexokinase activity in tomato fruit perturbs carbon and energy metabolism and reduces fruit and seed size. Plant Cell Envir. 27: 89-98. [b] Centeno et al. (2011) Malate plays a crucial role in starch metabolism, ripening, and soluble solid content of tomato fruit and affects postharvest softening. Plant Cell 23: 162-184. [c] Tiessen et al. (2002) Starch synthesis in potato tubers is regulated by post-translational redox modification of ADP-glucose pyrophosphorylase : a novel regulatory mechanism linking starch synthesis to the sucrose supply. Plant Cell 14: 2191-2213. [d] Roberts (1990) Observation of uridine triphosphate: glucose-1-phosphate uridyltransferase activity in maize root tips by saturation transfer ^{31}P-NMR. Estimation of cytoplasmic PPi. Biochim. Biophys. Acta 1051: 29-36.

Supplemental Table 2. Time-dependent function of relative growth rate, metabolites and enzyme capacities.*

Parameter	Time-dependent function	R^2
Relative growth rate (RGR)	0.1671/60/24*(1-1/(1+(92.3817/0.9055-1)*exp(-0.1671*(Time/24/60))))	0.83
Tissue density (d)	(7.75*10^-2*Time/24/60+13)/(7.75*10^-2*Time/24/60+12)	0.90
Starch	3.6068*10^-13*Time^3-5.3927*10^-8*Time^2+0.0019*Time+2.5371	0.80
Cell wall	3.9469*10^-13*Time^3-6.6146*10^-8*Time^2+2.4806*10^-3*Time+6.9355	0.75
V_{max} GK	-3.4885*10^-15*Time^3+6.2458*10^-10*Time^2-3.8249*10^-5*Time+0.8605	0.79
V_{max} FK	-6.7103*10^-15*Time^3+1.1894*10^-9*Time^2-6.9466*10^-5*Time+1.4057	0.89
V_{max} Susy	7.9541*10^-15*Time^3-1.1936*10^-9*Time^2+4.8084*10^-5*Time+0.0113	0.71
V_{max} NI	(3.8035*10^-16*Time^3-7.9214*10^-13*Time^2-3.0429*10^-6*Time+0.2028)/2	0.58
V_{max} AI	(2.5979*10^-14*Time^3-2.726*10^-9*Time^2+7.4956*10^-5*Time+0.2481)/2	0.75
V_{max} PGM	-2.9019*10^-14*Time^3+4.7246*10^-9*Time^2-2.7928*10^-4*Time+7.3772	0.86
V_{max} PGI	-1.0305*10^-14*Time^3+1.7290*10^-9*Time^2-9.9270*10^-5*Time+2.4434	0.92
V_{max} UGPase	-4.8047*10^-15*Time^3+5.7552*10^-10*Time^2-3.1225*10^-5*Time+3.9769	0.79
V_{max} PFK	-8.4421*10^-16*Time^3+1.4446*10^-10*Time^2-8.6909*10^-6*Time+0.2490	0.75
V_{max} PFP	-1.5405*10^-14*Time^3+2.6240*10^-9*Time^2-1.5537*10^-4*Time+3.7471	0.90
V_{max} ALD	(-5.1582*10^-14*Time^3+9.2647*10^-9*Time^2-5.4484*10^-4*Time+12.7342)/2	0.80
V_{max} SPS	1.2652*10^-15*Time^3-1.2248*10^-10*Time^2+3.4344*10^-6*Time+0.0483	0.51
V_{max} FBPase	-5.725*10^-18*Time^3+1.6521*10^-12*Time^2-2.0406*10^-7*Time+0.0185	0.79

* V_{max} values are expressed in µmol min^{-1} g^{-1} FW, *RGR* in min^{-1}, cell wall and starch content, in µmol of glucose equivalent g^{-1} FW. Tissue density, expressed in g FW mL^{-1}, was calculated from a linear fit of the time course of the fresh-to-dry weight ratio of pericarp. Parameters of the time-dependent functions have been obtained by least-square regression of the values measured on pericarp from 8 to 55-DPA aged tomato fruits (see Figure 1 and supplemental Figure 1). Enzyme abbreviations are the same as in Figure 2.

Supplemental Table 3. Enzymatic steps, reactions and equations rates of the kinetic model.

Enzyme / step	Reaction	Rate[§]	Rate equation
Glucokinase (GK)	GLC + ATP -> GLU6P + ADP	v2	Vm_HK_GLC*(GLCcyt/KmGLCcyt_HK_GLC)*(ATP/KmATP_HK_GLC)/((1.0+ATP/KmATP_HK_GLC)*(1.0+GLCcyt/KmGLCcyt_HK_GLC+FRUcyt/KmFRUcyt_HK_GLC+GLC6P/KiGLC6P_HK_GLC+FRU6P/KiFRU6P_HK_GLC))*d/Vcyt
Fructokinase (FK)	FRU + ATP -> FRU6P + ADP	v3	VmFRKa*FRUcyt*ATP/(KmATPfrka*FRUcyt+KmFRUfrka*ATP+FRUcyt*ATP)*d/Vcyt
Sucrose-6-phosphate synthase (SPS)	UDPGLC + FRU6P = UDP + S6P	v4	Vf_SPS*(FRU6P*UDPGLC-S6P*UDP/Keq_SPS)/(FRU6P*UDPGLC*(1.0+S6P/KiS6P_SPS)+KmFRU6P_SPS*(1.0+Phos/KiPi_SPS)*(UDPGLC+KiUDPGLC_SPS)+KmUDPGLC_SPS*FRU6P+Vf_SPS/(Vr_SPS*Keq_SPS)*(S6P*KmUDP_SPS*(1.0+UDPGLC/KiUDPGLC_SPS)+UDP*(KmS6P_SPS*(1.0+KmUDPGLC_SPS*FRU6P/(KiUDPGLC_SPS*KmFRU6P_SPS*(1.0+Phos/KiPi_SPS)))+S6P*(1.0+FRU6P/KiFRU6P_SPS))))*d /Vcyt
Sucrose-6-phosphatase	S6P -> SUC + Pi	v5	Vm_SPase*S6P/(KmS6P_SPase+S6P)*d/Vcyt
Sucrose synthase (Susy)	UDPGLC + FRU = UDP + SUC	v6	-VfSSc*(SUC*UDP-FRUcyt*UDPGLC/KeqSS)/(SUC*UDP*(1.0+FRUcyt/KiFRUssc)+KmSUCssc*(UDP+KiUDPssc)+KmUDPssc*SUC+VfSSc/(VrSSc*KeqSS)*(FRUcyt*KmUDPGLCssc*(1.0+UDP/KiUDPssc)+UDPGLC*(KmFRUssc*(1.0+KmUDPssc*SUC/(KiUDPssc*KmSUCssc))+FRUcyt*(1.0+SUC/KiSUCssc))))*d/Vcyt
Neutral invertase (NI)	SUC -> GLC + FRU	v7	Vm_NI/(1.0+GLCcyt/KiGLCcyt_NI)*SUC/(KmSUC_NI*(1.0+FRUcyt/KiFRUcyt_NI)+SUC)*d/Vcyt
ATP-dependent phosphofructokinase (PFK)	FRU6P + ATP -> FBP +ADP	v8	VmPFK*(FRU6P/FRU6Phalf)^hpfk*(ATP/ATPhalf)^hpfk/((1.0+(ATP/ModATPhalf)^hpfk)/(1.0+sigma^(4.0*hpfk)*(ATP/ModATPhalf)^hpfk)+(FRU6P/FRU6Phalf)^hpfk+(ATP/ATPhalf)^hpfk)*(1.0+sigma^(2.0*hpfk)*(ATP/ATPhalf)^hpfk)/(1.0+sigma^(4.0*hpfk)*(ATP/ATPhalf)^hpfk)+(FRU6P/FRU6Phalf)^hpfk)*(ATP/ATPhalf)^hpfk)*d/Vcyt
PPi-dependent phosphofructokinase (PFP)	FRU6P + PPi = FBP + Pi	v9	VmPFP/(KmFRU6Ppfp*KmPPipfp)*(FRU6P*PPi-FBP*Phos/KeqPFP)/((1.0+FRU6P/KmFRU6Ppfp+FBP/KmFBPpfp)*(1.0+PPi/KmPPipfp+Phos/KmPipfp))*d/Vcyt
Vacuolar Suc carrier	SUC = SUCvac	v10	(Vf10*SUC/Km10Suc-Vr10*SUCvac/Km10Sucvac)/(1.0+SUC/Km10Suc+SUCvac/Km10Sucvac)*d/Vcyt

Vacuolar acid invertase	SUCvac -> FRUvac + GLCvac	v11	Vm_AI/(1.0+GLCvac/KiGLCvac_NI)*SUCvac/(KmSUC_AI*(1.0+FRUvac/KiFRUvac_NI)+SUCvac)*d/Vvac
Sucrose storage	SUCvac -> SUC store	v12	RGR*SUCvac
Glucose storage	GLCvac -> GLC store	v13	RGR*GLCvac
Fructose storage	FRUvac -> FRU store	v14	RGR*FRUvac
Vacuolar Glc carrier	GLC = GLCvac	v15	(Vf16*GLCcyt/(Km16Glc+FRUcyt)-Vr16*GLCvac/(Km16Glcvac+FRUvac))/(1.0+GLCcyt/(Km16Glc+FRUcyt)+GLCvac/(Km16Glcvac+FRUvac))*d/Vcyt
Vacuolar Fru carrier	FRU = FRUvac	v16	(Vf16*FRUcyt/(Km16Glc+GLCcyt)-Vr16*FRUvac/(Km16Glcvac+GLCvac))/(1.0+FRUcyt/(Km16Glc+GLCcyt)+FRUvac/(Km16Glcvac+GLCvac))*d/Vcyt
Phosphoglucose isomerase (PGI)	GLC6P = FRU6P	v17	(Vf17*GLC6P/Km17G6P-Vr17*FRU6P/Km17F6P)/(1.0+GLC6P/Km17G6P+FRU6P/Km17F6P)*d/Vcyt
Phosphoglucomutase (PGM)	GLC6P = GLC1P	v18	(Vf18*GLC6P/Km18G6P-Vr18*GLC1P/Km18G1P)/(1.0+GLC6P/Km18G6P+GLC1P/Km18G1P)*d/Vcyt
UDP-gluco pyrophosphorylase (UGPase)	UTP + GLC1P = UDPGLC + PPi	v19	(Vf19*UTP*GLC1P/(Km19UTP*Km19G1P)-Vr19*UDPGLC*PPi/(Km19UDP*Km19PPi))/((1.0+UDPGLC/Km19UDPGLC+UTP/Km19UTP)*(1.0+PPi/Km19PPi+GLC1P/Km19G1P))*d/Vcyt
Aldolase (ALD)	FBP -> 2*TrP	v20	VmALD*FBP/(KmFBPALD+FBP)*d/Vcyt
Starch synthesis	GLC6P -> starch	v21	RGR*starch
Cell wall synthesis	GLC6P -> cell wall	v22	RGR*cell wall
Glc6P / Pi translocase	GLC6P + Piplast = GLC6Pplast + Pi	v23	Vf23/((Km23G6P)*Km23phosplast)*(GLC6P*Phosplast-GLC6Pplast*Phos/Keq23)/((1+GLC6P/Km23G6P+GLC6Pplast/Km23G6Pplast)*(1+Phosplast/Km23phosplast+Phos/Km23phos))* d /Vcyt
Fru-1,6-*bis*phosphatase (FBPase)	FBP -> FRU6P + Pi	v24	Vm_FBPase*FBP/(KmFBP+FBP)*d/Vcyt

Footnote: § Rates are expressed in mM min^{-1}. Enzyme abbreviations are the same as in Figure 2.

Supplemental Table 4. Enzymes, reactions and parameters of the kinetic model

Reaction & parameters	**Value** [§]	**Value range & references ***
Reaction 2: Glucokinase (GK)		
GLC + ATP -> GLC6P + ADP		
$V_{max}2$	Suppl. Table 2	this study
Km2Glc	0.07	0.03-0.13 [a]; 0.07 [b]; 0.02-0.13 [e]; 0.044 [c]
Km2Fru	10	17 [c] ; 2.3-3.2 [v] ; 7.7 [ad]
Km2ATP	0.25	0.1-0.56 [a]; 0.25 [b]
Ki2G6P	0.1	[a, b, e]
Ki2F6P	10	[a, b, e]
Reaction 3: Fructokinase (FK)		
FRU + ATP > FRU6P + ADP		
$V_{max}3$	Suppl. Table 2	this study
Km3Fru	0.028	0.04-0.22 [a] ; 0.028-0.074 [b]
Km3ATP	0.14	0.046-0.67 [a]; 0.14-0.18 [b]
Reaction 4: Sucrose-6-phosphate synthase (SPS)		
UDPGLC + FRU6P = S6P + UDP		
Keq4	10	5-10 [a, r]
$V_{max}4f$	0.065	$V_{max}r/V_{max}f$ = 1.9 [a]
$V_{max}4r$	0.125	this study
Km4F6P	0.6	0.3-2 [a]; 0.7-0.9 [aa]
Km4UDPGlc	1.8	1.2-3 [a]; 6.2-8 [aa]
Km4UDP	0.3	estimate [a, b]
Km4Suc6P	0.1	estimate [a, b]
Ki4Pi	3	0.2-85 [a, b]
Ki4F6P	0.4	estimate [a, b]
Ki4UDPGlc	1.4	estimate [a, b]; 9.1-9.7 [aa]
Ki4Suc6P	0.07	estimate [a, b]
Reaction 5: Sucrose-6-phosphatase		
S6P + H_2O -> SUC + Pi		
$V_{max}5$	0.125	estimate (non limiting) [a, b]
Km5Suc6P	0.1	0.045-0.15 [a, b]

Reaction 6: Sucrose synthase (Susy) **SUC + UDP = UDPGLC + FRU**		
Keq6	0.5	0.5 [b]; 0.15-0.56 [s]; 0.3-0.6 [z]
V_{max}6f	Suppl. Table 2	this study, with V_{max}f/V_{max}r = 0.25-0.35 [s, ag, ah]
Km6Suc	35.9	10-400 [b]; 33.6-38.2 [s]; 22-30 [z]; 31-108 [ac]; 53 [ag]; 22-65 [ah]
Km6UDP	0.00191	0.1-1.7 [b] 0.0019 [s] 0.0076-0.032 [z]0.07-0.26 [ac]0.019 [ag]0.03-0.07 [ah]
Km6UDPGlc	0.234	0.1-5 [b] 0.42-0.45 [z] 0.209-0.259 [s] 0.04-0.19 [ac] 0.09 [ag] 0.06-0.3 [ah]
Km6Fru	6.49	1.6-8 [b] 5.8-7.1 [s] 1.05-2.65 [z] 4.3-42 [ac] 8.4 [ag] 7-28 [ah]
Ki6Suc	139	140 [b]
Ki6Fru	3.1	4 [b]; 3.9-4.1 [s]; 25-169 [ac]
Ki6UDP	0.0871	0.3 [b]; 0.05-0.09 [ac]
Reaction 7: Neutral invertase (NI) **SUC + H_2O -> GLC + FRU**		
V_{max}7	Suppl. Table 2	this study
Km7Suc	10	10 [a, b]
Ki7Fru	15	15 [a, b, q]
Ki7Glc	15	15 [a, b, q]
Reaction 8: ATP-dependent phosphofructokinase (PFK) **FRU6P + ATP -> FBP + ADP**		
V_{max}8	Suppl. Table 2	this study
FBPhalf	0.758	[a, b]
ATPhalf	0.155	[b]
hPFK	2.3	[b]
ModATPhalf	2	[b]
sigma	0.9	[b]
Reaction 9: PPi-dependent phosphofructokinase (PFP) **FRU6P + PPi -> FBP + Pi**		
V_{max}9	Suppl. Table 2	this study
Keq9	3.3	[b]
Km9FBP	0.382	[b]; 0.139-0.21 [ae]
Km9FRU6P	1	[b]; 0.38-0.89 [ae]

Km9PPi	0.12	[b]; 0.017-0.033 [ae]
Km9Pi	0.51	[b]; 0.13-0.63 [ae]
Reaction 10: Vacuolar sucrose carrier **SUC = SUCvac**		
Keq10	1	
V_{max}10f	optimized	
V_{max}10r	$V_{max}10f .10^{-\Delta pH/2}$	ΔpH-driven active transport with an apparent Keq = $10^{\Delta pH}$
Km10Suc	1.2 , 12 or 120	10 [b]; 10.9-12.2 [h]; 21 [g]; 230 [ai]
Km10Sucvac	$Km10Suc.10^{\Delta pH/2}$	
Reaction 11: Vacuolar acid invertase (AI) **SUCvac + H_2O -> GLC + FRU**		
V_{max}11	Suppl. Table 2	this study
Ki11Glcvac	15	15 [a, b]; 37 [y]
Ki11Fruvac	15	15 [a, b]; 32.25 [y, q]
Km11Sucvac	10	10 [a, b], 7.97-10.1 [w]; 5-12 [x]; 11.3-19.9 [ab] ; 8 [af]
Reactions 15 & 16: Vacuolar hexose carrier **GLC = GLCvac** or **FRU = FRUvac**		
Keq15 = Keq16	1	
V_{max}15f = V_{max}16r	optimized	
V_{max}15r = V_{max}16r	$V_{max}15f .10^{-\Delta pH/2}$	ΔpH-driven active transport with an apparent Keq = $10^{\Delta pH}$
Km15Glc = Km16Fru	0.4 , 4 or 40	3.7 [p]; 120 [ai]
Km15Glcvac = Km16Fruvac	$Km15Glc.10^{\Delta pH/2}$	
Reaction 17: Phosphoglucose isomerase (PGI) **GLC6P = FRU6P**		
Keq17	0.31	0.3-0.32 [f]; 0.33 [i]
V_{max}17r	Suppl. Table S2	this study, with $V_{max}f/V_{max}r$ = 0.56 [f]; 0.34 [i]
Km17G6P	0.31	0.31 [f]; 1.07 [i]; 0.44-0.58 [ae]
Km17F6P	0.174	0.174 [f]; 0.12 [i]; 0.12-0.48 [ae]
Reaction 18: Phosphoglucomutase (PGM) **GLC6P = GLC1P**		
Keq18	0.05	0.052 [m]
V_{max}18r	Suppl. Table 2	this study

Km18G6P	0.3	estimate
Km18G1P	0.3	0.1-0.12 [k]; 0.06 [l]; 0.098 [k]; 0.02-0.12 [ae]
Reaction 19: UDPGlc pyrophosphorylase (UGPase)		
UTP + GLC1P = UDPGLC + PPi		
Keq19	0.15	
V_{max}19r	Suppl. Table 2	this study, with V_{max}f/V_{max}r = 1.16 [n]
Km19UDPGLC	0.5	0.72 [n]; 0.68 [af]; 0.04-0.26 [ae]
Km19UTP	0.1	0.14 [n]; 0.25 [u] ; 0.22 [af]; 0.22-0.56 [ae]
Km19PPi	0.15	0.15 [n] ; 0.56 [af]; 0.03-0.2 [ae]
Km19GLC1P	0.5	0.42 [n]; 0.33 [u]; 0.83 [af] ; 0.05-0.18 [ae]
Reaction 20: Aldolase (ALD)		
FBP -> glycolysis		
V_{max}20	Suppl. Table 2	this study
Km20FBP	0.015	0.002-0.02 [b, ae]
Reaction 23: Glc-6-P translocase		
GLC6P + Pi_plast = GLC6P_plast + Pi		
Keq23	1	
V_{max}23	0.2	estimate (non limiting)
Km23G6P	0.6	0.7-1.1 [l]; 0.3-0.33 [m]; 0.31-0.51 [ad]
Km23Pi	1.1	0.6-1.1 [l]; 0.18-0.25 [ad]
Km23G6Pplast	0.6	estimate
Km23phosplast	1.1	estimate
Reaction 24: Fru-1,6-*bis*phosphatase (FBPase)		
FBP -> FRU6P + Pi		
V_{max}24	Suppl. Table 2	this study
Km24FBP	0.1	0.02-0.013 [ae]

Footnotes : § Km and Ki are expressed in mM; V_{max}, in µmol min^{-1} g^{-1} FW. Enzyme abbreviations are the same as in Figure 2.

References: [a] Rohwer and Botha (2001) Analysis of sucrose accumulation in the sugar cane culm on the basis of in vitro kinetic data. Biochem. J. 358: 437-445. [b] Uys et al. (2007) Kinetic model of sucrose accumulation in maturing sugarcane culm tissue. Phytochem. 68: 2375-2392. [c] Dai et al. (1999) Overexpression of Arabidopsis hexokinase in tomato plants inhibits growth, reduces photosynthesis, and induces rapid senescence. Plant Cell 11: 1253-1266. [d] Gonzali et al. (2001) Characterization of two Arabidopsis thaliana fructokinases. Plant Sci. 160: 1107-1114. [e] Claeyssen and Rivoal (2007) Isozymes of plant hexokinase: occurrence. properties and functions. Phytochem. 68: 709-731. [f] Dyson and Noltmann (1968) The effect of pH and temperature on the kinetic parameters of

phosphoglucose isomerase. J. Biol. Chem. 243: 1401-1414. [g] Kaiser and Heber (1984) Sucrose transport into vacuoles isolated from barley mesophyll protoplasts. Planta 161: 562-568. [h] Weise et al. (2000) A new subfamily of sucrose transporters. SUT4. with low affinity / high affinity capacity localized in enucleate sieve elements of plants. Plant Cell 12: 1345-1355. [i] Staples and Suarez (1997) Honeybee flight muscle phosphoglucose isomerase matching enzyme capacities to flux requirements at near-equilibrium reaction. J. Biol. Chem. 200: 1247-1454. [j] Davies et al. (2003) Molecular and biochemical characterization of cytosolic phosphoglucomutase in wheat endosperm. J. Exp. Bot. 54: 1351-1360. [k] Periappuram et al. (2000) The plastidic phosphoglucomutase from Arabidopsis. A reversible enzyme reaction with an important role in metabolic control. Plant Physiol. 122: 1193-1199. [l] Esposito et al. (1999) Phosphoglucomutase activity during development of wheat grains. J. Plant Physiol. 154: 24-29. [m] Farré et al. (2001) Analysis of the compartmentation of glycolytic intermediates, nucleotides, sugars, organic acids, amino acids, and sugar alcohols in potato tubers using a nonaqueous fractionation method. Plant Physiol. 127: 685-700. [n] Litterer et al. (2006) Characterization and expression of Arabidopsis UDP-sugar pyrophosphorylase. Plant Physiol. Biochem. 44: 171-180. [o] Wormit et al. (2006) Molecular identification and physiological characterization of a novel monosaccharide transporter from *Arabidopsis* involved in vacuolar sugar transport. Plant Cell 18: 3476-3490. [p] Aluri and Buttner (2007) Identification and functional expression of the *Arabidopsis thaliana* vacuolar glucose transporter 1 and its role in seed germination and flowering. PNAS 104: 2537-2542. [q] Sturm (1999) Invertases. Primary Structures. Functions. and Roles in Plant Development and Sucrose Partitioning. Plant Physiol. 121: 1-8. [r] Lunn and ap Rees (1990) Apparent equilibrium constant and mass-action ratio for sucrose-phosphate synthase in seeds of Pisum sativum. Biochem. J. 267: 739-743. [s] Schafer et al (2005) Partial purification and characterization of sucrose synthase in sugarcane. J. Plant Physiol. 162: 11-20. [t] Schafer et al (2004) A kinetic study of sugarcane sucrose synthase. Eur. J. Biochem 271: 3971-3977. [u] Decker et al. (2012) Substrate kinetics and substrate effects on the quaternary structure of barley UDP-glucose pyrophosphorylase. Phytochem. 79: 39-45. [v] Kandel-Kfir et al. (2006) Two newly identified membrane-associated and plastidic tomato HXKs: characteristics, predicted structure and intracellular localization. Planta 224: 1341-1352. [w] Wang et al. (2005) Vacuolar invertases in sweet potato: Molecular cloning, characterization and analysis of gene expression J. Agricult. Food Chem. 53: 3672-3678. [x] Tang et al. (1996) Purification and characterisation of soluble invertases from leaves of Arabidopsis thaliana. Planta 198: 17-23. [y] Sampietro et al. (1980) A regulatory invertase from sugar cane leaf-sheaths. Phytochem. 19: 1637-1642 [z] Matic et al. (2003) Sucrose synthase isoforms in cultured tobacco cells. Plant Physiol. Biochem. 42: 299-306 [aa] Harbron et al. (1981) The purification and properties of Sucrose-Phosphate Synthetase from Spinach Leaves: The Involvement of this Enzyme and Fructose Bisphosphatase in the regulation of Sucrose Biosynthesis. Arch. Biochem. Biophys. 212: 237-246. [ab] Nägele et al. (2010) Mathematical modeling of the central carbohydrate metabolism in arabidopsis reveals a substantial regulatory influence of vacuolar invertase on whole plant carbon metabolism. Plant Physiol. 153: 260-272. [ac] Bieniawska et al. (2007) Analysis of the sucrose synthase gene family in Arabidopsis. Plant J. 49: 810-828. [ad] Menu et al. (2001) Cloning and characterization of a cDNA encoding hexokinase from tomato. Plant Sci. 160: 209-218. [ae] http://www.brenda-enzymes.org. [af] Yelle et al. (1991) Sink metabolism in tomato fruit. IV- genetic and biochemical analysis of sucrose accumulation. Plant Physiol. 95: 1026-1035. [ag] Sun et al. (1992) Sucrose synthase in wild tomato, *Lycopersicon chmielewskii*, and tomato fruit sink strength. Plant Physiol. 98: 1163-1169. [ah] Suzuki et al. (1996) Occurrence of two sucrose synthase isozymes during maturation of Japonese pear fruit. J. Amer. Soc. Hort. Sci. 121: 943-947. [ai] Milner et al. (1995) Properties of proton and sugar transport at the tonoplast of tomato (*Lycopersicon esculentum*) fruit. Physiol. Plantarum 94: 399-410.

Supplemental Table 5. Ordinary Differential Equations (ODE) corresponding to the network of Figure 2*.

Intermediate	ODE
Cytoplasmic fructose	$dFRU\_cyt/dt = V7 - V16 - V3 - V6 = (V_{cyt}*v7 - V_{cyt}*v16 - V_{cyt}*v3 - V_{cyt}*v6)/d$
Vacuolar fructose	$dFRU\_vac/dt = V16 + V11 - V14 = (V_{cyt}*v16 + V_{vac}*v11 - V_{vac}*v14)/d$
Cytoplasmic glucose	$dGLC\_cyt/dt = V7 - V15 - V2 = (V_{cyt}*v7 - V_{cyt}*v15 - V_{cyt}*v2)/d$
Vacuolar glucose	$dGLC\_vac/dt = V15 + V11 - V13 = (V_{cyt}*v15 + V_{vac}*v11 - V_{vac}*v13)/d$
Cytoplasmic sucrose	$dSUC\_cyt/dt = V1 + V5 + V6 - V7 - V10 = V1 + (V_{cyt}*v5 + V_{cyt}*v6 - V_{cyt}*v7 - V_{cyt}*v10)/d$
Vacuolar sucrose	$dSUC\_vac/dt = V10 - V11 - V12 = (V_{cyt}*v10 - V_{vac}*v11 - V_{vac}*v12)/d$
Sucrose-6-P	$dS6P/dt = V4 - V5 = (V_{cyt}*v4 - V_{cyt}*v5)/d$
Cytoplasmic glucose-6-P	$dGLC6P/dt = V2 - V18 - V23 - V17 = (V_{cyt}*v2 - V_{cyt}*v18 - V_{cyt}*v23 - V_{cyt}*v17)/d$
Plastidial glucose-6-P	$dGLC6P\_plast/dt = V23 - V21 = (V_{cyt}*v23 - V_{plast}*v21)/d$
Fructose-6-P	$dFRU6P/dt = V3 + V17 + V24 - V4 - V8 - V9 = (V_{cyt}*v3 + V_{cyt}*v17 + V_{cyt}*v24 - V_{cyt}*v4 - V_{cyt}*v8 - V_{cyt}*v9)/d$
Glucose-1-P	$dG1P/dt = V18 - V19 = (V_{cyt}*v18 - V_{cyt}*v19)/d$
UDP-glucose	$dUDPGLC/dt = V19 - V6 - V4 - V22 = (V_{cyt}*v19 - V_{cyt}*v6 - V_{cyt}*v4 - V_{cyt}*v22)/d$
Fructose-1,6-*bis*P	$dFBP/dt = V8 + V9 - V24 - V20 = (V_{cyt}*v8 + V_{cyt}*v9 - V_{cyt}*v24 - V_{cyt}*v20)/d$

*V_i are fluxes, expressed in µmol min^{-1} g^{-1} FW; v_i , reaction rates, expressed in mM min^{-1} (see supplemental Table 3); $V_{vac,}$ V_{cyt} and V_{plast} , the volume fraction of vacuole, cytoplasm and plastid, respectively and *d*, the tissue density (see supplemental Table 1).